ME401 - Semester Project

Measurement Methods for FireHorn I Exhaust Emissions During Horizontal Propulsion Test

written by

Haroun Naina (289169)
Master SGM - Semester II

supervised by

Mathieu Udriot
Systems Engineer in Sustainable Space
EPFL Space Center

School of Engineering
École Polytechnique Fédéral de Lausanne

June 2025

Contents

List of Figures

List of Tables

1 Introduction

1.1 General Context

The fast expansion of the space industry raises growing concerns about its environmental footprint, especially as launch frequencies continue to rise globally. Among the key contributors to this impact is rocket exhaust, whose chemical composition depends on several parameters, including the type of propulsion system, its operating conditions, and the nature of the propellants used. These emissions interact with various atmospheric layers in complex and sometimes long-lasting ways. Depending on the altitude and mission profile, they may lead to the release of persistent pollutants such as black carbon or alumina particles, which can remain in the stratosphere or mesosphere for extended periods, influencing atmospheric chemistry and potentially accelerating climate change. Beyond direct exhaust gases, the broader ecological cost of space missions includes additional factors such as the toxicity and environmental hazards of certain propellants, the carbon footprint and energy demands of their production processes, as well as the risks associated with their storage, handling, and accidental release. Furthermore, the accumulation of space debris and the potential contamination of ecosystems near launch and test sites have become increasingly pressing issues. Together, these challenges highlight the necessity of developing robust, data-driven methodologies for evaluating the comprehensive environmental impact of space-related activities.

This report presents the work conducted as part of a semester project within the Master's program in Mechanical Engineering at EPFL. The objective of the project is to design, based on available existing data, two distinct measurement systems aimed at quantifying the chemical composition of the exhaust gases emitted by the FireHorn I rocket engine developed by the EPFL Rocket Team. These systems are based on two fundamentally different approaches. The first approach consists of extracting exhaust gas samples directly from the plume via a probe inserted into the exhaust zone. This probe is connected to a conduction network that simultaneously cools the gas and transports it to a hermetically sealed storage receptacle. This method enables the collection of unaltered gas samples for post-test laboratory analysis and allows for a theoretical characterization of the rockets ecological impact. The second approach involves observing the post-burnout exhaust jet using infrared imaging systems positioned at a depth where they remain unaffected by the flow field. This method allows for the real-time visualization of the interaction between the exhaust gases and the ambient atmosphere, thereby enabling a direct assessment of the environmental impact under actual operating conditions.

Although both systems ultimately aim to assess the ecological footprint of the rocket, their respective measurement targets differ: one focuses on the pure exhaust gas composition, while the other captures a composition influenced by ambient environmental conditions. As such, an initial neutral evaluation of both systems, independent of any specific application context, is proposed in order to enable an objective comparison. Subsequently, the impact of the experimental context on the global performance of each system is analyzed to identify which design is most appropriate under context-related constraints.

The structure of this report is subdivided in six main sections. Section 1 (Introduction) outlines the general context of the project, the operational constraints related to the horizontal test bench, as well as the scope and limitations of the study. Section 2 (Literature Review) presents a comprehensive overview of the composition of exhaust gases from both solid and liquid rocket motors, the environmental impact of these propulsion systems, and various methods used to assess such impacts. Section 3 (Methodology) details the approach followed for (i) the design and budgeting method of the two measurement systems and (ii) the assessment method applied to compare them. Section 4 (Results) presents the results obtained from the dimensioning methodology, including the characteristic parameters of each design, their estimated budgets, and their evaluation scores. Section 5 (Analysis) provides a critical review of all major findings, including the methodology employed, the budget implications, and the assessment outcomes. Finally, Section 6 (Conclusion) summarizes the project objectives, key results, identified limitations and assumptions, and proposes recommendations for future work.

1.2 Case of Study

1.2.1 Launch Vehicle (Firehorn I)

This study focuses on the cryogenic bi-liquid propulsion system of the Firehorn I, a single-stage launch vehicle developed by the EPFL Rocket Team with a constant internal diameter of 240 mm. Designed for participation in the 2025 edition of the European Rocketry Challenge (EuRoC), the Firehorn I operates on ethalox, a propellant mixture composed of ethanol (C_2H_5OH) as fuel and liquid oxygen (LOX) as oxidizer.

Due to the cryogenic nature of the oxidizer, the system requires careful storage and handling at extremely low temperatures. The engine provides an average thrust of approximately 7 kN, allowing the rocket to reach a target apogee of 9 ± 0.45 km under nominal flight conditions. In addition to propulsion performance, the mission architecture must satisfy two critical constraints: the recovery of the main rocket body after flight and the successful transport of a scientific payload in the form of a CubeSat with a total mass ranging between 1000 and 1330 grams. A detailed description of the launcher is presented on figure 1 and table 1.

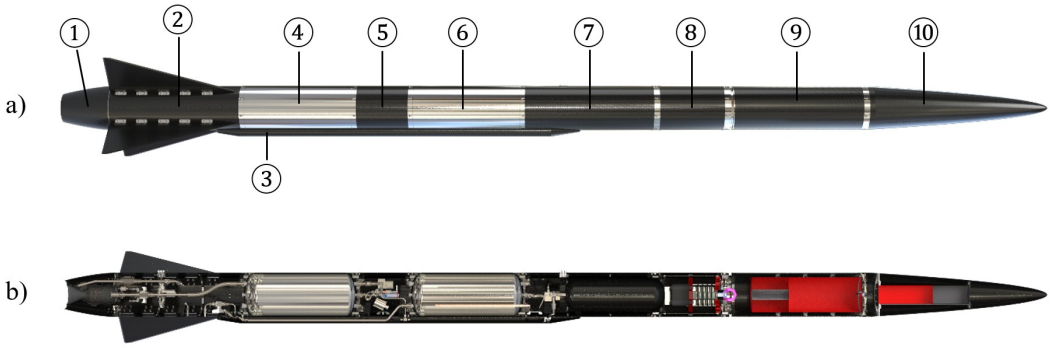

Figure 1: Firehorn I a) Render b) Cut view

1	Boattail	Length : 295 mm ; Mass : 3.40 kg
2	Engine Bay	Length : 700 mm ; Mass : 16.20 kg
3	Aerocover	Length : 2122 mm ; Mass : 1.65 kg
4	LOx Tank	Length : 622 mm ; Mass : 7.40 kg ; Propellant : 24.80 kg
5	Midbay	Length : 280 mm ; Mass : 5.70 kg
6	ETH Tank	Length : 522 mm ; Mass : 7.40 kg ; Propellant : 17.10 kg
7	Pressurant Bay	Length : 755 mm ; Mass : 13.20 kg ; Pressurant : 3.00 kg
8	Avionics Bay	Length : 395 mm ; Mass : 8.50 kg
9	Recovery Bay	Length : 775 mm ; Mass : 13.20 kg
10	Nosecone	Length : 1000 mm ; Mass : 5.60 kg
	Firehorn I	**Length : 5465 mm ; Mass : 80.80 kg**

Table 1: Firehorn I dimensions

Following Firehorn I, a second iteration, named Firehorn II, is under development. This upgraded version aims to reach a significantly higher target apogee of 30 km. To achieve this performance, Firehorn II will be equipped with a more powerful thruster delivering 12 kN of thrust. Additionally, it will carry larger propellant tanks increasing from 25 L on Firehorn I to 60 L and a greater amount of pressurant, from 3 kg to 9 kg. The overall structure of the rocket will also be significantly larger, in order to accommodate these upgrades and endure the higher thermal and mechanical loads associated with this increased performance.

1.2.2 Testing Facility

The testing facility is located approximately 15 km from the EPFL campus, in the municipality of Savigny. The facility is composed of a test bench, a restricted area during testing, a control zone, and a spectator area, as illustrated in Figure 2.

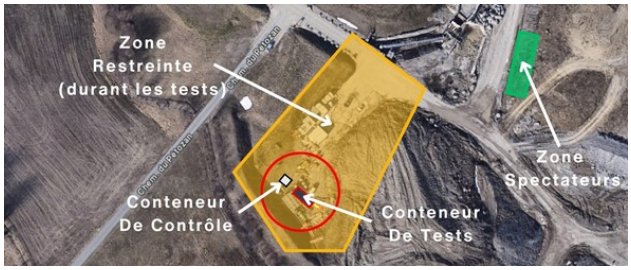

Figure 2: Site Composition

The ground surface of the facility consists of gravelly sand. The test bench comprises a thrust stand designed for horizontal testing of the propulsion system, as well as storage tanks for fuels, oxidizers, and nitrogen pressurization. These tanks are interconnected through valves acting as actuators and control elements, which are remotely operated from the control zone. Additionally, the tanks are equipped with sensors to ensure their monitoring and control. An illustration of the propellant feed system is shown on figure 3.

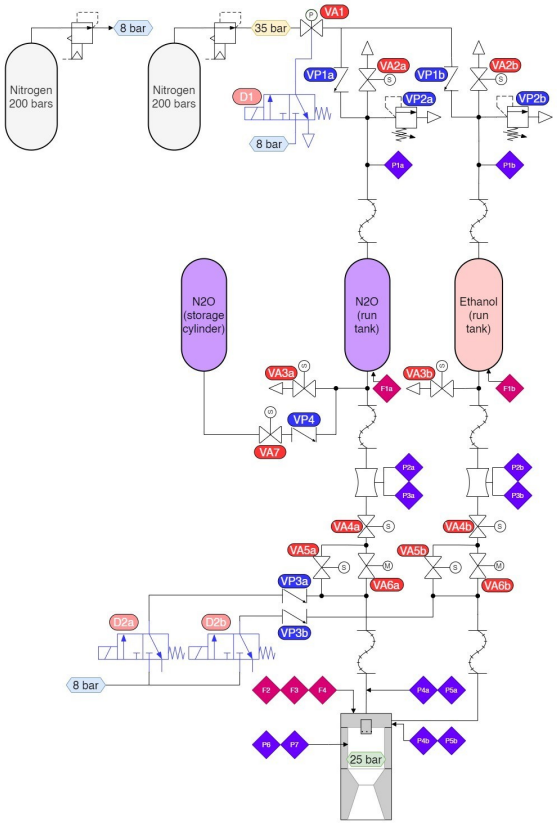

Lab.	Comp.	Funct.
P1	Pressure	Run tank pressure
P2	Pressure	Venturi inlet
P3	Pressure	Venturi outlet
P4	Pressure	Manifold DC
P5	Pressure	Manifold AC
P6	Pressure	Combustion chamber DC
P7	Pressure	Combustion chamber AC
F1	Force	Run tanks weight
F2	Force	Engine thrust 1
F3	Force	Engine thrust 2
F4	Force	Engine thrust 3
VA1	Valve	Run tank pressurization main
VA2	Valve	Run tank vent
VA3	Valve	Run tank purge
VA4	Valve	Main line safety redundancy
VA5	Valve	Ignition bypass
VA6	Valve	Main flow control
VA7	Valve	Filling
VP1	Valve	Pressurization checkvalve
VP2	Valve	Run tank pressure relief
VP3	Valve	Line purge check valve
VP4	Valve	Filling check valve

Figure 3: Schematic of the test facility's plumbing network (left) and its corresponding table of components (right)

The thrust stand is fitted with sensors to measure the performance of the propulsion system during tests. Furthermore, the entire test bench is equipped with cameras providing real-time video feedback accessible from the control zone. A CAD representation of the container is displayed on figure 4

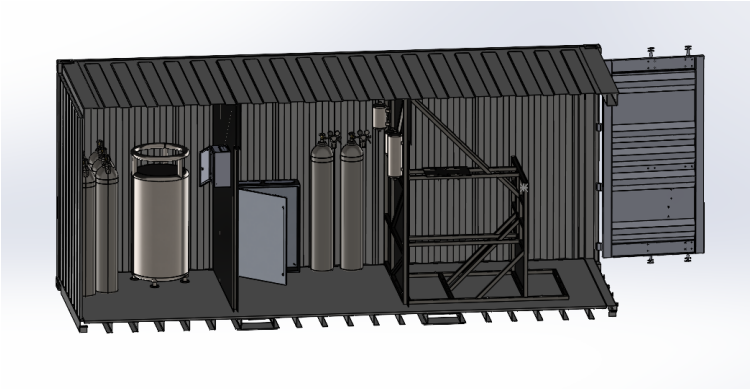

Figure 4: CAD representation of the test bench (section view)

1.3 Main Objectives

The primary objective of this project is to design two measurement system that can quantify the chemical composition of rocket exhaust gases generated by the FireHorn I rocket engine developed by the EPFL Rocket Team. The long-term goal is to provide precise characterization of the rockets ecological footprint through experimental data using the measurement system designed in this project.

While both approaches intend to evaluate the ecological footprint of rocket propulsion, they differ in their scope. The first design targets a detailed analysis of the exhaust gas composition itself, the second approach focuses on capturing data influenced by ambient environmental conditions. A comprehensive comparative evaluation of these systems is undertaken to identify which method provides superior applicability under specific operational constraints.

1.4 Scope and limitation of study

Both of the measurement systems are intended for integration into the horizontal propulsion test bench of the FireHorn I launcher. These systems are conceived to operate in parallel with rocket firing tests. The scope of this project is limited to the conceptual and dimensional design of both systems; no physical realization or prototyping is conducted. The objective is to propose a preliminary sizing methodology capable of generating results that can later be refined through more accurate simulations or experimental validation.

Due to the lack of pre-existing experimental data related to the exhaust gaz, the entire design process is based on computational tools, external publications, and referenced datasets. Specifically, the flow conditions, such as velocity field, temperature distribution, shock wave location, and the flow stabilization zone, are extracted from a precomputed CFD simulation. The chemical composition and thermodynamic properties of the exhaust gas are obtained from a Rocket Propulsion Analysis (RPA) simulation, which estimates these parameters based on engine-specific input data. The input parameters for both the CFD and RPA simulations are assumed to be consistent and representative of the FireHorn I propulsion unit.

The budget estimation for each design is carried out independently of the actual operational and financial constraints specific to the EPFL Rocket Team or the EuRoC context. Since the financial planning for such systems must often precede funding approval, the budgeting methodology adopted here prioritizes completeness and conservatism over strict cost optimization. Reference tables and industrial estimates are used wherever possible to account for various cost components. As a result, the final cost evaluations are deliberately overestimated to provide a safe upper bound, which may later be revised downwards depending on the practical implementation context.

2 Literature Review

The rapid growth of the space industry has led to increasing concerns regarding its environmental impact. The ecological footprint of space activities is influenced by a wide range of factors and can be analyzed from multiple perspectives. One primary determinant is the composition of rocket exhaust, which depends on the type of propulsion system, its operating regime, and the propellants used. The production of distinct emissions depending of thruster properties influence atmospheric chemistry and contribute to various environmental effects.

Beyond the primary emissions from combustion, the environmental impact of space missions is also shaped by the interaction between exhaust plumes and atmospheric constituents. This interaction is highly dependent on the altitude at which emissions are released, as well as the specific mission profile, including maximum altitude and atmospheric residence time of exhaust products. Certain pollutants, such as black carbon and alumina particles, may remain in the stratosphere or mesosphere for extended periods, amplifying their climatic and chemical effects.

Furthermore, the ecological footprint of space missions extends beyond exhaust emissions. Additional factors, such as the environmental cost of propellant (i.e. the toxicity of certain propellants, the release of ozone-depleting substances, the carbon footprint of production processes, and the contamination risks associated with storage and handling), launcher production, as well as the release of debris into the atmosphere or orbit, must also be considered. The accumulation of space debris and the potential contamination of ecosystems near launch sites further emphasize the need for a comprehensive assessment of the industry's environmental impact.

Given the complexity and multifaceted nature of these challenges, it is essential to examine the various existing methodologies for evaluating the ecological footprint of space activities. The objective of this state-of-the-art review is to present the key environmental challenges associated with different characteristics of space missions, providing a reference framework for analyzing the results of this project.

2.1 Rocket Propulsion and Exhaust Gas Composition

Rocket propulsion systems are broadly classified into two main categories: Solid Rocket Motors (SRMs) and Liquid Rocket Engines (LREs). In addition to these, Hybrid Rocket Engines (HREs) combine features of both, using a liquid or gaseous oxidizer with a solid fuel. These hybrid engines are often encountered in academic projects. Each of these propulsion technologies has distinct characteristics in terms of fuel composition, operational behavior, and environmental impact.

SRMs use solid aluminum as a fuel and ammonium perchlorate (NH_4ClO_4) as an oxidizer. Modern formulations also incorporate hydroxyl-terminated polybutadiene (HTPB) to enhance performance. These engines offer advantages such as easy storability, high reliability, and simple design. However, they operate at a constant thrust level that cannot be adjusted once ignited, nor stopped, making them particularly suitable for use as boosters in the initial and final phases of a launch. The exhaust emissions of SRMs pose significant environmental concerns. The combustion process releases hydrogen chloride (HCl), which contributes to atmospheric acidification, and aluminum oxide (Al_2O_3) particles, which can remain in the upper atmosphere for extended periods[1–3]. These emissions contribute to ozone depletion and radiative forcing, with SRMs exhibiting a radiative forcing value of 0.18 mW/m^2 per launch per year, primarily due to aluminum particle emissions[4].

LREs utilize liquid propellants, where both the fuel and oxidizer are stored separately and mixed during combustion. The most commonly used combinations include, first, RP-1 (Kerosene) as fuel and Liquid Oxygen (LOx) as oxidizer. This combination is widely used in the initial stages of launches due to the high density of RP-1, which minimizes the required storage volume. However, kerosene-fueled engines produce substantial carbon dioxide (CO_2) and black carbon (soot) emissions, both of which contribute to global warming[4–8]. Research[4] have shown that these engines exhibit a significant CO_2 radiative forcing of 6 Œ 10^{-6} mW/m^2 per launch per year, while black carbon emissions result in a total radiative forcing of 0.32

mW/m^2 per launch per year, making kerosene-fueled LREs one of the most environmentally concerning propulsion systems[8–10].
Another commonly used LRE propellant is Liquid Hydrogen (H_2) as fuel and Liquid Oxygen (LOx) as oxidizer. Unlike kerosene, hydrogen has a very low density, requiring large storage tanks in cryogenic conditions, which is why LH_2/LOx combinations are often used in upper-stage propulsion systems. The primary advantage of hydrogen-fueled LREs is the absence of CO_2 emissions. However, their exhaust is composed mainly of water vapor, which significantly contributes to radiative forcing[5]. These engines exhibit a water vapor radiative forcing of 0.02 mW/m^2 per launch per year, a value higher than most other propellants (<0.05 mW/m^2)[4].
Studies on alimenting the LRE system with Unsymmetrical Dimethylhydrazine (UDMH) and Dinitrogen Tetroxide (N_3O_4), known as hypergolic propellant, highlighted other interesting properties. This highly reactive propellant ignites spontaneously upon contact with an appropriate oxidizer[11], eliminating the need for an ignition system and reducing design complexity. Hypergolic engines are typically used in applications where high-precision orbital maneuvering is required. These propellants can be stored for long periods, making them advantageous for extended missions[5]. However, they are also highly toxic; the combination of nitric acid and UDMH is referred to as "Devils Venom" due to its severe environmental and health hazards[5,12,13].

Recent advancements have led to the development of hybrid propulsion systems, which combine characteristics of both SRMs and LREs. Hybrid engines exhibit an exhaust composition consisting of 28% aluminum particles, 70% black carbon, and 2% water vapor[4]. These systems aim to optimize performance while mitigating some of the environmental drawbacks of traditional propulsion methods[14].

Numerical simulations have been conducted[15] to analyze the 70-meter-long exhaust plume of a SpaceX Raptor2 engine, which operates on a methane-based propellant (LOx-LCH_4). These simulations aimed to quantify the oxidation of CO $\rightarrow$ CO_2 and hydrocarbons $\rightarrow$ H_2O, CO_2, as well as to study the dynamic evolution of NOx emissions. The results indicate a high concentration of carbon monoxide (CO) in the initial phase of the exhaust plume, which is almost entirely converted into carbon dioxide (CO_2) through interaction with ambient air. Additionally, the oxidation of unburned methane residues occurs extremely rapidly, with lifetimes of less than 1 millisecond. After 433 milliseconds, the simulations estimate that the exhaust plume, upon reaching 70 meters, undergoes substantial mixing with ambient air at a rate of 196 127 kg/s. This mixing process results in emissions of: NO: 2.55 kg/s, CO: 1.17 kg/s and CO_2: 545.44 kg/s
Add a small section about propulsion systems used most often by (student) sounding rocket, suborbital launch vehicles (to compare against orbital, larger launch vehicles)

2.2 Environmental Impact of Rocket Emission

2.2.1 Ozone Depletion

The assessment of the impact of space missions on the Earth's ozone layer is conducted by analyzing both local and global effects. Local effects refer to environmental changes occurring near the launch site and in the lower atmosphere, while global effects encompass the broader impact on the entire atmospheric system beyond the launch area.

SRMs have been identified as significant contributors to local ozone depletion. A study[16] measured a 40% reduction in ozone levels within the exhaust plume of a Titan III launch in the lower stratosphere. Further research in 1997[17,18] investigated the exhaust plume of a Titan IV launch, revealing high concentrations of molecular chlorine (Cl_2) over an 8 km plume, formed through the interaction between hydrogen chloride (HCl) in the SRM exhaust and ambient air. The study also found that ozone concentrations within the plume closely matched ambient ozone levels during nighttime launches, suggesting that night launches cause less ozone depletion in the stratosphere compared to daytime launches. This difference is attributed to the absence of UV radiation at night, which otherwise catalyses ozone loss reactions by bringing the the activation energy needed. Additional studies[16–21] have reported total ozone depletion within an 8 km exhaust plume, with ozone concentrations dropping to 0% within 30 to 60 minutes after launch. Another study[22] measured ozone concentrations ranging from 0% to 30% in the exhaust plume of a Delta II rocket

for up to 39 minutes post-launch, while yet another study[23] observed an ozone hole caused by an Ariane V launch lasting up to four days.

Compared to SRMs, LREs have a significantly lower impact on local atmospheric chemistry[24], as they release fewer reactive chemicals and particulate emissions. However, the most notable environmental concern associated with LREs is black carbon emissions, primarily from kerosene-fueled engines (RP-1/LOx). Black carbon contributes to radiative forcing and potential disruptions to stratospheric ozone chemistry[4,8,19], though its effects remain less severe than those of SRM exhaust.

Another significant local environmental concern is the ground cloud formed near launch sites. A study[25] described the formation of low-pH (<0.5) acid liquid droplet following the coagulation of atomized water and alumina particle. These ground clouds present environmental hazards in the lower troposphere, where HCl emissions acidify nearby water sources, threatening marine ecosystems[25–29]. Studies have observed localized damage to flora and fauna[29–32], caused by acid rain[33] and exhaust toxic particle deposition[34]. Research[34] has determined a total deposition area of 0.23 km^2. A density of 0-127 g/m^2 and 0-246 g/m^2 has been found on 0.126 km^2 around launch site. While the current low frequency of space launches limits their long-term impact, the expected increase in launch frequency could disrupt ecosystem regeneration and potentially compromise local food chains.

On a global scale, the chlorine derived from HCl conversion in SRM exhaust plumes can act as a catalyst for ozone depletion[35], significantly affecting the overall ozone layer and atmospheric chemistry[36]. A study[35] estimated that 15 annual SRM launches could result in a 0.025% reduction in global ozone levels, without considering localized ozone losses. Additionally, research[37] has shown that localized ozone depletion caused by chlorine within the SRM exhaust wake is an order of magnitude smaller than the long-term global ozone reduction driven by catalytic chlorine reactions.

The global impact of aluminum oxide (Al2O3) particles has also been studied. Without accounting for localized effects, annual spaceflight activity is estimated to contribute to a 0.025% reduction in global ozone levels per year[1], with one-third of this depletion attributed to aluminum oxide particles and two-thirds to chlorine emissions[38].

Regarding nitrogen and water vapor emissions, their impact on global ozone depletion is lower but still existent. A study[39] analyzing 10 Proton launches using hypergolic LREs (UDMH/N2O4) found that the resulting nitrogen and water vapor emissions caused a global ozone reduction of less than 0.001%, suggesting that these emissions pose a relatively minor threat, even considering the expected increase in launch frequency. Also, a study[39] modeled the ozone loss caused by H_2O and NOx emission from hypergolic engine and found that most of the loss were caused by NOx emission. Additionally, hypergolic LREs exhibit relatively low water vapor radiative forcing.

A study[40] has quantified the scale of emissions from space launches for year 2023. The total emissions up to 100 km altitude were estimated at 7.13 Œ 10^4 t, with 52% of these emissions concentrated within the first 20 km of altitude. The emissions in this range included 54.7% CO2, 28.1% H2O, 8% CO, 4.9% N_2, and less than 4% black carbon. Notably, CO_2 concentration decreases above 50 km, indicating reduced interaction between the exhaust plume and ambient air. The overall environmental impact of these emissions has been estimated at 5.05 to 9.35 Œ 10^7 kg CO_2-eq, with 41% of the impact attributed to CO_2 emissions and 56% to black carbon. For comparison, total emissions and environmental impact from global aviation in 2018 were estimated at 2.85 Œ 10^{11} kg of CO2 emissions and 1.79 Œ 10^{12} kg CO2-eq, meaning that the space industry contributed 0.0052% of global emissions and 0.0226% of the global environmental impact.

2.2.2 Mesopheric Clouds

Another significant environmental aspect that is linked to exhaust from space launches is the formation of mesospheric clouds[5,41–45]. These are the highest-altitude clouds in Earth's atmosphere, forming in the mesosphere due to the presence of water vapor[46]. Mesospheric clouds can influence radiative forcing, potentially

affecting the Earth's energy balance. A study[47] observed an increase in mesospheric radiation levels over a 10-month period following the launch of four rockets powered by LRE systems. Additionally, large-scale rocket activity could significantly impact mesospheric cloud coverage. A study[48] recorded a local increase of 22% in cloud cover following a single launch. The polar regions are particularly susceptible to mesospheric cloud formation, as lower temperatures and atmospheric dynamics favor cloud nucleation in these areas[49]. This sensitivity raises concerns about potential climate impacts, especially as the frequency of space launches continues to rise.

2.2.3 Re-entry

Another critical environmental concern associated with space activities is the pollution caused by the re-entry of unused spacecraft components into the atmosphere. The disposal of these debris in the ocean can disrupt marine ecosystems, as re-entering components often contain residual toxic and carcinogenic propellants. A study[50] reported that 3040 kg of unburned UDMH (Unsymmetrical Dimethylhydrazine) were found in debris falling back to Earth after re-entry. In contrast, kerosene poses a lower risk of marine toxicity due to its rapid evaporation[51], making it less persistent compared to UDMH-based fuels.

As of 2023, 9,855.5 tons of artificial objects are currently orbiting Earth[52], with only a fraction being functional[53]. That year, 200 spacecraft re-entries were recorded, totaling 451.4 tons of mass. The composition of these re-entering materials included 60.3% Al2O3 (aluminum oxide), 22.7% NOx, 5.6% CO, 5.5% MgAl2O4 (magnesium aluminate), and 2.6% TiO_2 (titanium dioxide). The total mass of debris re-entering the Earth's atmosphere was 195.8 tons, further emphasizing the growing concern of orbital debris pollution.

In addition to material deposition, re-entering components at high velocities generate a form of pollution known as "re-entry shockwave pollution". The extreme thermal energy experienced by objects re-entering Earth's atmosphere excites atmospheres oxygen (O2) and nitrogen (N2) molecules, leading to the formation of nitrogen oxides (NOx)[54–56]. The severity of this process is highly dependent on the geometry of the object, its trajectory, and the re-entry angle. A study[57] determined that a mass of NOx corresponding to 17.5% of the structural mass of the vehicle is formed in re-entry, while another study[58] determined a percentage of 37.5%. Observations[54] indicate that this phenomenon typically occurs at altitudes of 5590 km for objects re-entering at speeds exceeding 5 km/s. The peak emissions of NOx occur in the mesosphere and are subsequently transported into the stratosphere, where they influence ozone concentration levels.

A growing concern is the increasing number of satellite constellation debris, which could double the annual injection of aerosol particles into the mesosphere[59]. This would result in a higher accumulation of aluminum particles in the stratosphere[60], potentially exacerbating long-term atmospheric changes.

2.3 Methods for Assessing Rocket Emission

The first assessments of the space industry's environmental impact, dating back to 1957, were based on historical data. However, these early evaluations highlighted a significant lack of information, demonstrating the need for more comprehensive methods to study rocket emissions and their ecological consequences. Today, the study of rocket exhaust can be conducted using a variety of approaches, including mathematical models[61,62], numerical simulations[15], and real-time in-situ measurements[16,62]. Additionally, some studies[40] rely on databases to assess specific environmental impacts, such as the GCAT[63] database, which provides data on vehicles re-entering Earth's atmosphere.

Among the commonly used mathematical models, the NRLMSIS model[64] is widely employed to simulate atmospheric conditions at different altitudes. Specific models have also been developed to estimate particular emissions: James et al.[65] proposed a model for black carbon emissions, while Park et al.[66] developed a model to estimate nitrogen oxide (NOx) production. Several computational tools are available for analyzing post-combustion processes and trajectory modeling: The NASA CEA[67] (Chemical Equilibrium with Applications) tool calculates exhaust emissions, atmospheric composition, and mass flow ratios for a

given rocket system; The ESA DRAMA SARA tool enables trajectory simulations and mass loss estimations based on user-defined input parameters.

Numerical simulations offer a detailed analysis of rocket exhaust dynamics, providing insights into both flow behavior and chemical reactions. Notable simulation models include: VIPER Parabolic Navier-Stokes Model[68] (Simulates the kinetic expansion of exhaust gases from the combustion chamber to the nozzle exit), PERCOP Model[69] (Models oxidizer-to-fuel ratio variations along the nozzle, with its accuracy evaluated by comparing results against VIPER simulations), SPF Model[70] (Simulates the structure of the exhaust flow and its interaction with ambient air. Studies have reported numerical instabilities, particularly in the barrel shock region) and TDK Model (Focuses on chemical reactions within the exhaust plume, providing insights into species formation and pollutant dispersion).

Beyond direct emissions analysis, several studies adopt the Life Cycle Assessment (LCA) methodology to evaluate the broader ecological impact of space missions. One widely used resource is the Strathclyde Space Systems Database (SSSD), a database validated by the European Space Agency (ESA). This database integrates data from Ecoinvent and ELCD inventories, making it a valuable tool for assessing environmental footprints specific to space projects.

3 Methodology

3.1 Preliminary Results and Data

The design and sizing of the systems presented in the following sections require a comprehensive understanding of the mechanical and chemical conditions present in the exhaust zone. The physical properties and chemical composition of the exhaust gas are estimated using a Rocket Propulsion Analysis (RPA) simulation. This simulation takes as input engine parameters (nominal thrust, chamber pressure), propellant characteristics (oxidizer/fuel), and nozzle properties (expansion area ratio, nozzle inlet condition) to determine, as output, the thermodynamic properties and chemical composition of the exhaust gas. A summary of the results that will be used for the subsequent stages of the project is presented in Table 2. The screenshots containing the complete results are presented in the appendix.

INPUT

Chamber Pressure [MPa]	2.5
Nominal Thrust [kN]	10
Ambient Pressure [MPa]	0.101325
Mixture Ratio (O/F) [-]	1.6
Oxidizer	O_2(L)
Fuel	C_2H_5OH(L)
Contraction Area Ratio [-]	5.0
Expansion Area Ratio [-]	5.6

OUTPUT (Nozzle Exit)

C_p [J/kgK]	2431.4
C_v [J/kgK]	2061.5
γ [-]	1.1794
M [g/mol]	23.9
$R_s = \frac{R}{M}$ [J/kgK]	347.8
ρ [kg/m^3]	0.09
μ [kg/ms]	8.134×10^{-5}
k [W/mK]	0.3263
Pr [-]	0.6061

Species	Mole Fraction
CO	0.191
CO_2	0.208
H	0.002
H_2	0.087
H_2O	0.509
O	$0.030 \cdot 10^{-3}$
O_2	$0.075 \cdot 10^{-3}$
OH	0.002

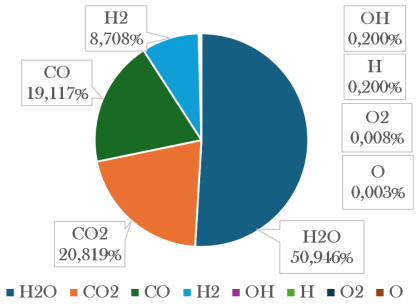

Table 2: Inputs and results of the Rocket Propulsion Analysis (RPA) simulation. In the OUTPUT section, the left column lists thermodynamic properties, the middle shows the detailed molefraction table, and the right displays a pie chart of the gas composition at the nozzle exit.

The velocity and temperature fields in the exhaust zone are obtained by exploiting Computational Fluid Dynamics CFD results (2D contours) performed previously as part of an other semester project for the ERT[71]. Temperature and Mach number data in the exhaust zone (along flow axis) will be extracted in order to approximate the flow velocity as follows:

$$\text{Ma} = \frac{U_\infty}{c} = \frac{U_\infty}{\sqrt{\gamma RT/M}} \Longrightarrow U_\infty = \text{Ma}\sqrt{\frac{\gamma RT}{M}} = \text{Ma}\sqrt{\gamma R_s T}$$

Where γ is the adiabatic index ($\gamma = \frac{C_P}{C_V}$, where C_P and C_V are the specific heats of the gas at constant pressure and volume, respectively), R is the ideal gas constant, and M is the molar mass. The adiabatic index and the ratio $\frac{R}{M}$ (corresponding to the specific gas constant for the exhaust gas) are provided by the RPA simulation. This process is illustrated on figure 5. The script used for this process is presented in appendix.

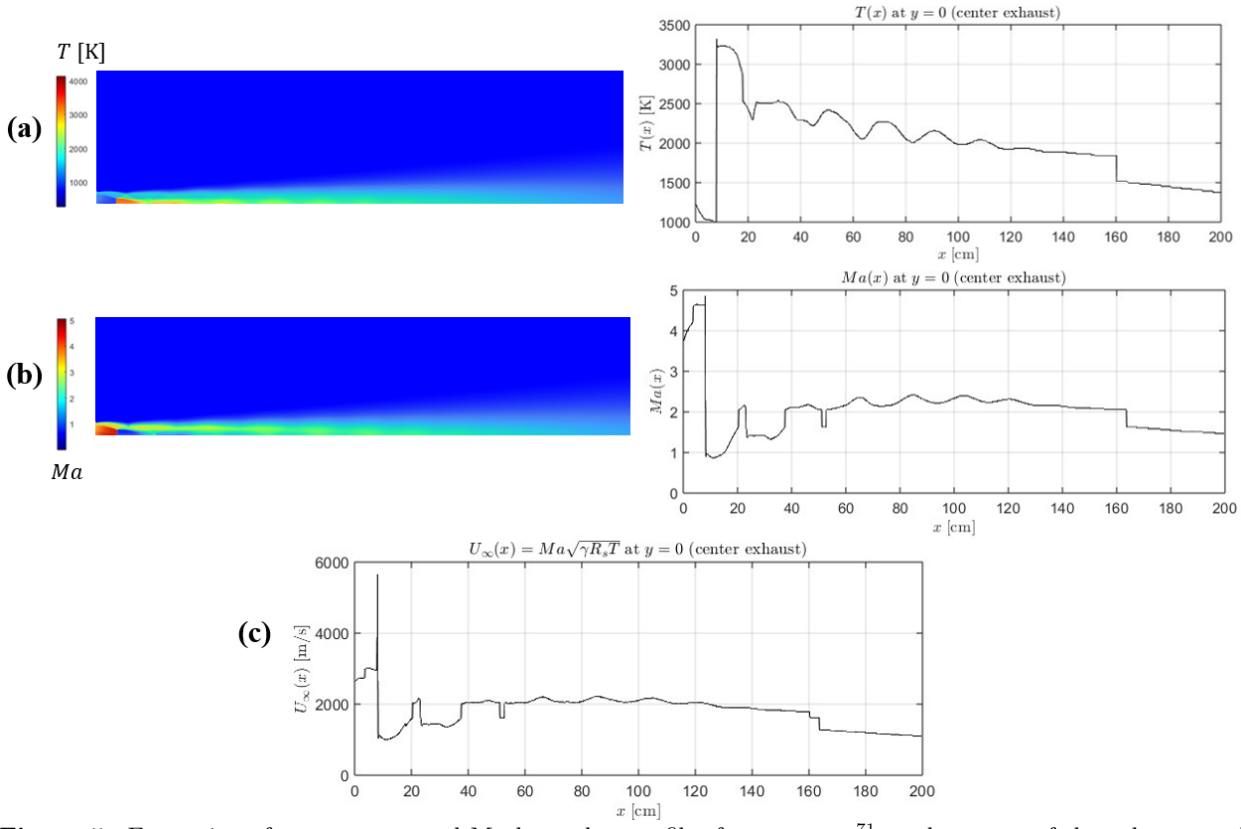

Figure 5: Extraction of temperature and Mach number profiles from contour[71] at the center of the exhaust, and subsequent velocity calculation: **(a)** Contour of static temperature $T(x, y)$ with the centerline profile $T(x)$ at $y = 0$ **(b)** Contour of Mach number $\mathrm{Ma}(x, y)$ with the centerline profile $\mathrm{Ma}(x)$ at $y = 0$. **(c)** Computed centerline velocity $U_\infty(x)$ plotted as a function of x at $y = 0$.

The spatial distributions of velocity and temperature as functions of height are illustrated in Figure 6:

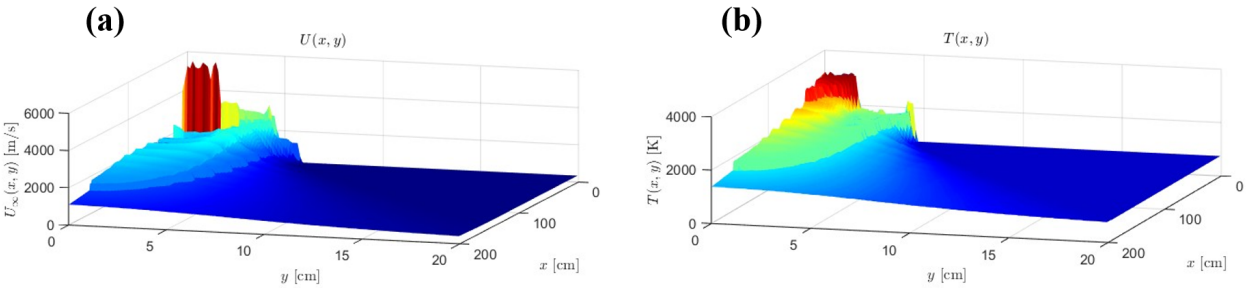

Figure 6: Three-dimensional plots of **(a)** the flow velocity $U(x, y)$ [m/s] and **(b)** the static temperature $T(x, y)$ [K] in the exhaust plume, shown as functions of vertical height y and distance from propulsion engine x.

The curves in figure 5 show that the shock wave is located in the range $x \in [6, 8]$ cm. At this location, the Mach number drops from $\mathrm{Ma} \simeq 4.84$ to $\mathrm{Ma} \simeq 0.89$. This drop is characterized by an increase in temperature, from $T \simeq 1015$ K to $T \simeq 3321$ K. Using these boundary values, the corresponding minimum and maximum velocity values are calculated to be $U_{\infty,\min} \simeq 650$ m/s and $U_{\infty,\max} \simeq 5649$ m/s, respectively, at the shock wave boundaries.

Additionally, a stable velocity is observed approximately 40 cm after the shock transition, in the range $x \in [40, 160]$ cm. As for the temperature in this region, it oscillates in a damped manner: starting from a maximum temperature of $T \simeq 2507$ K at a distance of 20 cm, it converges towards a minimum value of $T = 1844$ K. On the other hand, the Mach number oscillates between $Ma = 2.4$ and $\mathrm{Ma} \simeq 2.2$ for $x \in [40, 160]$ cm. Both oscillation lead to a stable velocity of $\overline{U}_\infty \simeq 2000$ m/s in this range.

Beyond this stable region, for $x > 160$ cm, a decrease in Mach number, temperature, and consequently velocity is observed. This drop could be caused by the significant dilution of both temperature and Mach number at larger distances from the propulsion system, resulting in a larger color gradient. This, in turn, increases the sensitivity to resolution when extracting and associating the colors to numerical values.

3.2 Design 1 : Sampling Probe

The principle of the first design consists of acquiring and storing a pure sample of exhaust gas during the test, to be analyzed in the laboratory after the test.

To achieve this, the acquisition of the exhaust gas requires, first, the design of a probe that will be placed in the extreme conditions of the jet. The primary and most dominant constraint is related to the high temperatures, as well as the mechanical forces required to secure the probe against aerodynamic forces. Once the probe design is established, the next step involves designing and analyzing a gas conduction system that will transport the exhaust gas to a sealed storage container. The system will be evaluated to determine the necessary hydraulic equipment, such as pumps, to ensure proper handling of the gas.
Finally, considering the chemical composition of the exhaust gas presented in Table 2, a cooling system for the gas must be incorporated to prevent any unintended chain reactions resulting from the high temperatures of the jet exhaust.

Based on the critical aspects mentioned for the design of this system, it is noted that the materials used must have a high melting point temperature, T_{melt}, to withstand the combustion jet temperature, a high yield strength, σ_{max}, to endure the aerodynamic forces, and good thermal conductivity, k, to facilitate the cooling of the gas. Therefore, a list of potential refractory metals selected based on these criteria is presented in table 3. A schematic drawing of this first system is presented in figure 7.

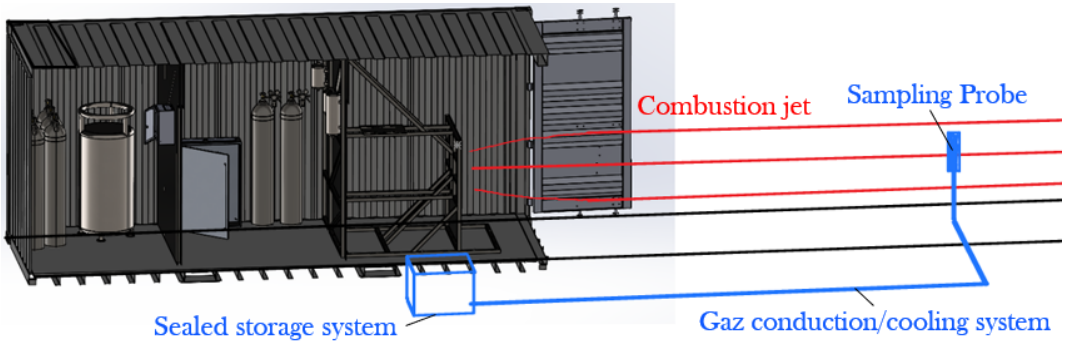

Figure 7: Illustration of the first system design

Material	T_{melt} [K]	σ_{Y} [MPa]	k [W/m K]	E [GPa]	ν	ρ [kg/m^3]	P [$/kg]
Tungsten (W)	3695	1506	178.0	410	0.26	19264	35.30
Rhenium (Re)	3459	1561	48.0	463	0.30	21010	3580.00
Osmium (Os)	3306	2814	87.6	548	0.25	22450	1 922 040.00
Tantalum (Ta)	3290	180	57.5	186	0.34	16650	305.00
Molybdenum (Mo)	2896	855	138.0	330	0.31	10200	40.10
Niobium (Nb)	2740	94	52.0	103	0.40	8570	73.50
Rhodium (Rh)	1965	687.4	150.0	380	0.26	12400	147 000.00
Chromium (Cr)	2133	387.9	69.1	140	0.21	7190	9.40

Table 3: List of potential refractory metals with yield strength values [72–93]

3.2.1 Structural Analysis

The structural analysis of this system is simplified by considering that only a portion of the system is exposed to the jet and the forces arising from it. In this regard, only the sampling probe is subjected to the jet, while the gas conduction system is buried underground, directing the gas to the storage system, which is located outside the exhaust zone. Based on this type of setup, the study of the mechanical forces exerted by the jet on the sampling probe can be reduced to a simple case of a cantilever beam subjected to a distributed load. The distributed load corresponds to the drag force divided by the length of the beam, as given by the following equation:

$$q = \frac{F_D}{L} = \frac{1}{2}\rho U_\infty^2 C_D A \cdot \frac{1}{L}$$

where ρ and U_∞ are defined in Section 3.1, C_D is the drag coefficient, and A is the reference area given by $A = DL$, where D and L are the diameter and length of the sampling probe, respectively. The experimental drag coefficient, C_D, as a function of the Reynolds number for a cylinder, is shown in figure 8[94]. By selecting a diameter of 0.16 m and considering that the probe will be set in the stable region where $U_\infty = \overline{U}_\infty = 2000$ m/s, we calculate a Reynolds number of $\text{Re} = \frac{\rho U_\infty D}{\mu} = 3.5 \cdot 10^5$. We can read on figure 8 that, for this Reynolds number, the flow is in the transition from a laminar to a turbulent boundary layers. This indicates that the drag coefficient has a high sensitivity to the flow velocity in that Reynold number range : it can fluctuate from $C_D = 0.6$ to $C_D = 0.3$, which yields a drag force fluctuating between $F_D = 27648$ N and $F_D = 13824$ N. Therefore, to conservatively estimate the drag force, we opt for the upper limit of $F_D = 27648$ N for the structural analysis.

This theoretical result has been verified numerically by performing a CFD simulation as displayed on figure 9, which calculates a drag force converging to $F_{D,\text{num}} \simeq 23,000$ N, representing an underestimation of approximately $\Delta F_D \simeq 16\%$ compared to the upper limit of the theoretically calculated drag force. The mesh and residuals leading to these results are presented in the appendix.

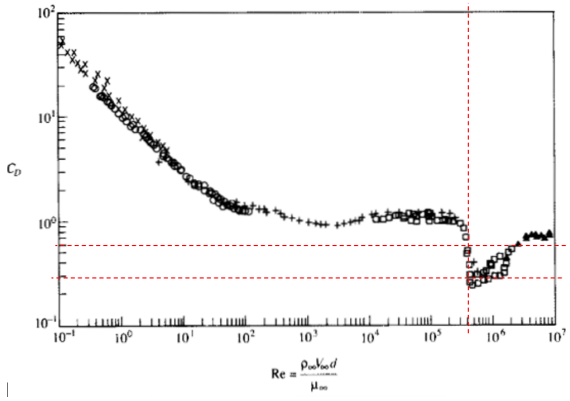

Figure 8: Cylinder drag coefficient C_D as a function of the Reynolds number Re [94]

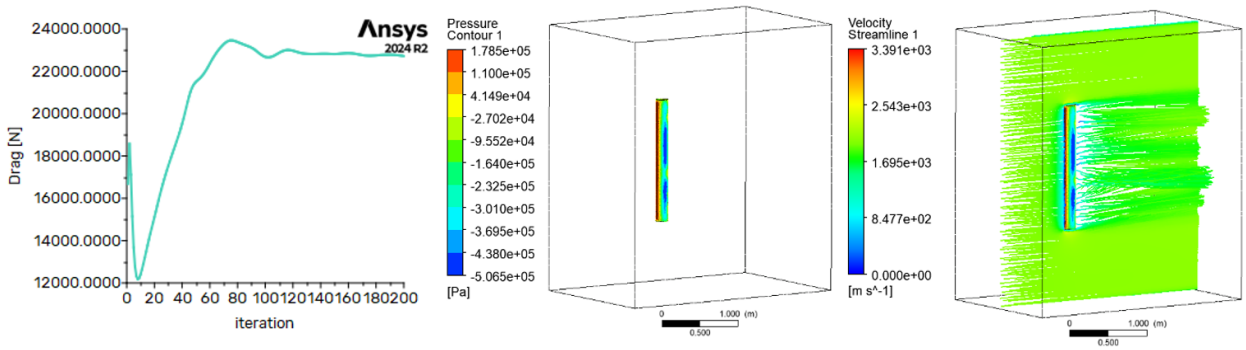

Figure 9: CFD simulation results of the probe drag force calculation

With a drag force of $F_D = 27638$ N, we calculate the distributed load as $q = \frac{F_D}{L} = 17280$ N/m. By fixing one end of the probe and applying this distributed load along the entire length of the cylinder, we can numerically determine the maximum stress, $\sigma_{\max}$, which will be used to assess the probes resistance to aerodynamic forces.

Figure 10 shows the displacement and the maximum principal stress field for the probe made of tungsten.

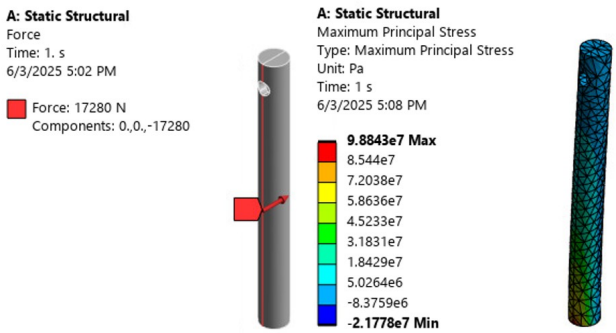

Figure 10: Maximum principal stress (σ_{Max}) from the structural simulation of the sampling probe in tungsten exposed to a uniform uniaxial exhaust flow of $\overline{U} = 2000$ m/s. **(left)** Boundary Condition **(right)** Maximum principal stress Field $\sigma_{\max}$ distribution, showing the peak stress near the clamped support

3.2.2 Counter-Flow Heat Exchager Analysis

In order to study the gas in its purest chemical composition, it is essential to prevent unwanted chemical reactions between combustion products after the gas has exited the exhaust. Indeed, observing the combustion products listed in Table 2, we can highlight several chain reactions that occur at very high temperatures, such as:

$$H_2 + \frac{1}{2}O_2 \leftrightarrow H_2O$$
$$O + H_2 \leftrightarrow OH + H$$
$$N_2 + O \leftrightarrow 2NO$$
$$CO + OH \leftrightarrow CO_2 + H$$
$$OH + H \leftrightarrow H_2O$$

Therefore, the goal of this section is to size the necessary length of a counter-flow heat exchanger that will lower the temperature from $T_{\text{hi}} = 2500$ K to $T_{\text{ho}} = 1200$ K, thus limiting unwanted chemical reactions.
For the cooling gas, nitrogen in its gaseous state is chosen, with an initial temperature of $T_{\text{ci}} = 100$ K. This choice avoids the phase change of liquid nitrogen, which occurs at a boiling temperature of ∼77 K. Properties of Nitrogen gas at 100 K are given by [95] and are repertoried in the following table :

Property	Value
ρ_c [kg/m^3]	3.44
C_{pc} [J/kgK]	1070.00
μ_c [Pa·s]	$68.80 \cdot 10^{-7}$
ν_c [m^2/s]	$2.00 \cdot 10^{-6}$
k_c [W/mK]	$9.58 \cdot 10^{-3}$
Pr_c	0.768

Table 4: Thermodynamic properties of nitrogen gas at 100 K [95]

The thermal flux in a counter-flow heat exchanger under steady-state conditions is given by:

$$\dot{Q}_{\text{c-f}} = UA \cdot \Delta T_{\text{lm}} = UA \cdot \frac{(T_{\text{ho}} - T_{\text{ci}}) - (T_{\text{hi}} - T_{\text{co}})}{\ln\left(\frac{(T_{\text{ho}} - T_{\text{ci}})}{(T_{\text{hi}} - T_{\text{co}})}\right)} \tag{1}$$

Where T_{co} is the temperature of the cooling gas exit and UA is the overall heat transfer coefficient, which corresponds to the sum of thermal resistances:

$$\frac{1}{UA} = \frac{1}{h_c \pi D_o L} + \frac{\ln(D_o/D_i)}{2\pi k_W L} + \frac{1}{h_h \pi D_i L} \tag{2}$$

Here, h_c and h_h are the convection heat transfer coefficients for nitrogen and exhaust gas, respectively, and L is the length of the conduit to be determined. Plugging 2 into 1 let us determine the expression for the length of the tube :

$$L = \frac{\dot{Q}_{\text{c-f}}}{\Delta T_{\text{lm}}} \left(\frac{1}{h_c \pi D_o} + \frac{\ln(D_o/D_i)}{2\pi k_W} + \frac{1}{h_h \pi D_i} \right) \tag{3}$$

Thus, the calculation of L depends on several factors, including T_{co}, h_c and h_h, which are yet to be determined.

The determination of the cooling gas exit temperature, T_{co}, is based on the conservation of energy. The heat emitted by the exhaust gas, $\dot{Q}_h$, is equal to the heat received by the cooling gas, $\dot{Q}_c$. By equating the energy for both fluids, we can determine a function $T_{\text{co}}(\dot{m}_c)$, which characterizes the cooling fluid exit temperature as a function of its mass flow rate:

$$\dot{Q}_h = \dot{Q}_c \Leftrightarrow \dot{m}_h C_{p,h}(T_{\text{hi}} - T_{\text{ho}}) = \dot{m}_c C_{p,c}(T_{\text{co}} - T_{\text{ci}}) \Longrightarrow T_{\text{co}}(\dot{m}_c) = \frac{\dot{m}_h C_{p,h}}{\dot{m}_c C_{p,c}}(T_{\text{hi}} - T_{\text{ho}}) + T_{\text{ci}}$$

Thus, the graph in figure 11 relates the cooling liquid exit temperature to its mass flow rate in the system, ensuring thermal exchange to cool the exhaust gas to the temperature T_{ho}. For a first estimation, we fix the mass flow rate at $\dot{m}_c = 2.5$ kg/s, resulting in an exit temperature of $T_{\text{co}} = 671.96$ K.

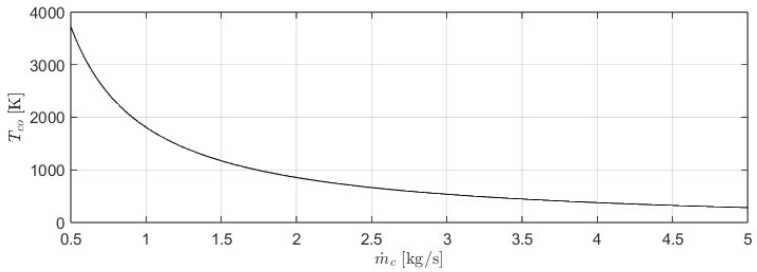

Figure 11: Outlet temperature of the Nitrogen cooling gas as a function of its inlet flow $T_{co}(\dot{m}_c)$

Regarding the convection coefficients h_c and h_h, their determination can be achieved using the Nusselt number and the correlation corresponding to our flow type. Here, we choose the Dittus-Boelter correlation, adapted for internal pipe flows. However, it is noted that this correlation is generally not recommended for large temperature differences and industrial applications, where pipe roughness affects the accuracy of the correlation[96]. Thus, we have:

$$\text{Nu}_D = 0.023 \cdot \text{Re}_D^{4/5} \text{Pr}^n = \frac{hD}{k} \tag{4}$$

With the Reynolds number $\text{Re}_D = \frac{\rho U D}{\mu}$, the Prandtl number Pr, and $n = 0.3$ for the hot gas and $n = 0.4$ for the cooling gas, we determine the convection coefficients $h_h = 1212.6$ W/m^{2}K for the exhaust gas and $h_c = 682.23$ W/m^{2}K for the cooling gas.

Thus, plugging now the known value of T_{co}, h_h and h_c, we compute a total pipe length of $L = 13.6 \simeq 14$ m.

3.2.3 Gas Conduction Analysis

The design of the gas conduction system requires understanding the behavior of the gas flow from its entry into the sampling probe to its exit toward the storage container. Indeed, the insertion of a component, such as a pump, to assist the gas in reaching its storage device depends on the limiting velocity of the gas within the conduit, which in turn is influenced by the length of the conduit (and thus the positioning of the sampling probe). This relationship is critical for sizing the system to ensure efficient gas transfer while maintaining appropriate flow characteristics.

To determine the gas exit velocity, we use Bernoullis equation, simplifying by neglecting the height difference between the entry and exit points ($z_{\text{in}} = z_{\text{out}}$) and accounting for pressure losses due to friction ΔP_L and elbows ΔP_c in the system. The resulting equation is:

$$P_{\text{atm}} + \rho g z_{\text{out}} + \frac{\rho U_{\text{out}}^2}{2} = P_{\text{atm}} + \rho g z_{\text{in}} + \frac{\rho U_\infty^2}{2} - \Delta P_L - \Delta P_c$$

Simplifying, we obtain the equation for the gas velocity at the exit:

$$\frac{\rho U_{\text{out}}^2}{2} = \frac{\rho U_\infty^2}{2} - \Delta P_L - \Delta P_c \Longrightarrow U_{\text{out}} = \sqrt{U_\infty^2 - \frac{2}{\rho}\left(\Delta P_L + \Delta P_c\right)} \tag{5}$$

Where ΔP_L is approximated using Darcy-Weisbach's equation, and ΔP_c is expressed using a loss factor K, which depends on the type and angle of the elbow. For a regular flanged pipe, the loss factor is approximated as $K_L \simeq 0.3$ for a 90 degree elbow[97]. The pressure losses are given by the following expressions:

$$\Delta P_L = \frac{f L \rho U_\infty^2}{2Dg} \quad \text{and} \quad \Delta P_c = \sum_i K_i \frac{\rho U_\infty^2}{2} = 3(0.3) \cdot \frac{\rho U_\infty^2}{2} \tag{6}$$

Where f is the friction factor which can be approximated using the Colebrook-White equation:

$$f = \frac{0.25}{\left[\log\left(\frac{\varepsilon}{3.7D} + \frac{5.74}{Re^{0.9}}\right)\right]^2}$$

In this equation, ε represents the average surface roughness. For a first estimation, we consider $\varepsilon \simeq 11.35\ \mu$m, which is a high roughness value for a tungsten surface[98]. With this assumption, we calculate a friction factor of $f \simeq 0.017$, which can be verified using the Moody diagram presented on figure 12. The relative roughness is given by $\varepsilon/D = 1.4 \cdot 10^{-4}$, and the Reynolds number is calculated as $Re = \frac{\rho U_\infty D}{\mu} = 1.7 \cdot 10^5$.

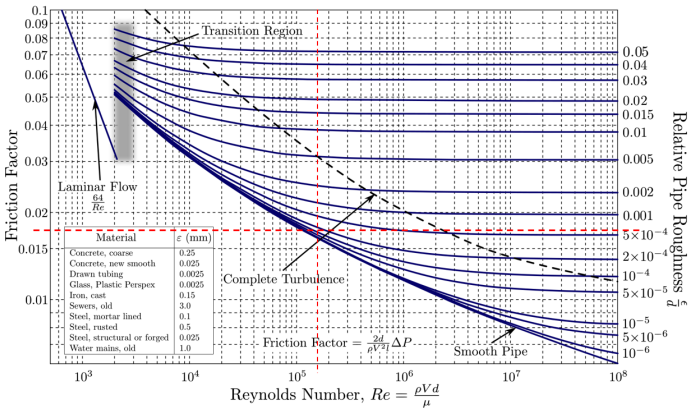

Figure 12: Moody Diagram for the conduction pipe friction factor [99]

By inserting the various values mentioned in equation 6 and considering a length $L = 14$ m as computed in the previous section, we calculate a pressure loss due to the bends $\Delta P_c = 162.0$ MPa and a friction loss of $\Delta P_L = 4.4$ Pa. Using 5, we determine an exit velocity of $U_{\text{out}} \simeq 1923.3$ m/s.

The theoretical result obtained was validated numerically, as presented in figure 13, where it can be observed that for both probe positions, the exit velocity appears to be very minimally affected by the pressure losses.

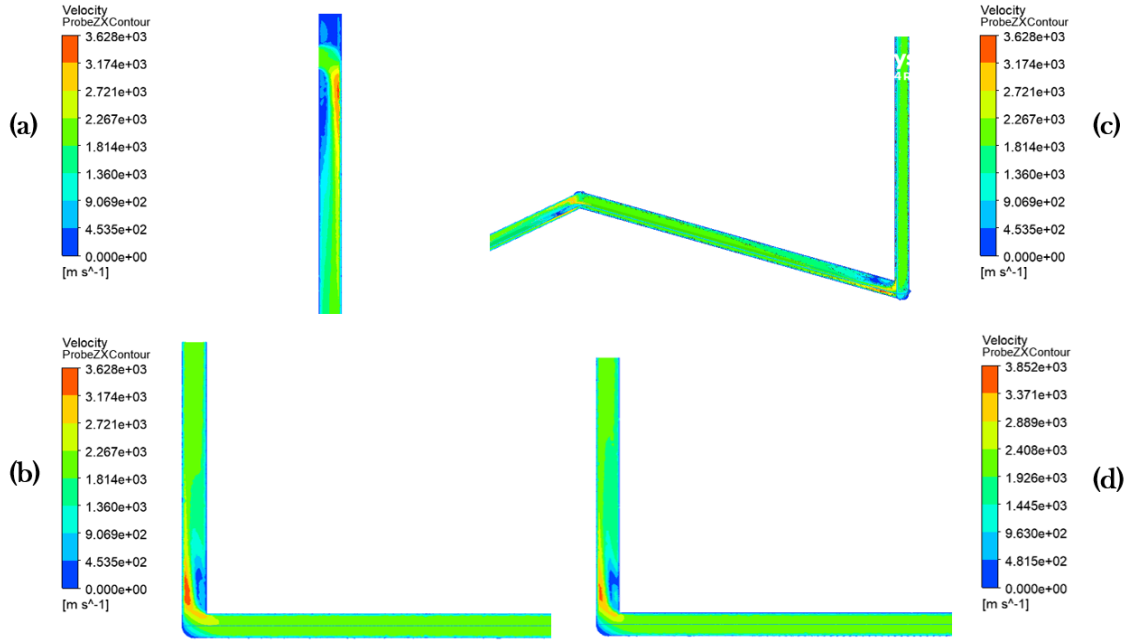

Figure 13: Velocity contours of the sampling probe system: **a)** Probe entry; **c)** Pressure losses across the first two elbows; **b)** Exit velocity contours for the probe positioned at 60 cm from the reactor; **d)** Exit velocity contours for the probe positioned at 160 cm from the reactor

3.2.4 Budget 1

The budget estimation for Design 1 is determined by three cost categories: (1) material production costs, (2) system installation costs and (3) labor cost. For a preliminary approximation of material costs, the total mass of each system component (i.e., the conduction piping and the cooling enclosure) is computed from its volume and material density. Specifically, the mass m of a component with outer diameter D_o, inner diameter D_i, and axial length L is given by

$$m \;=\; \rho\, A\, L \;=\; \rho\, \frac{\pi}{4}\,(D_o - D_i)^2\, L \;=\; \rho\, V,$$

Where ρ denotes the material density and V its volume. Once m is known, the production cost is obtained via

$$\mathrm{Cost}_{\mathrm{production}} \;=\; m \cdot \mathrm{Price}_{\mathrm{per\,kg}},$$

with the unit price per kilogram taken from Table 3.

Subsequently, installation costs, which encompass both excavation and system placement, are estimated using historical data provided by the intermediary firm *Ofri*[100]. Table 5 summarizes the average rates for professional construction and agricultural services, derived from *Ofri*s past project offers. These prices are applied to the required excavation volume and the length of piping to yield a estimate of installation costs.

Service	Unit	Cost from [CHF]	Cost to [CHF]
Site setup installation	Lump sum	300 .-	600 .-
Access road preparation	Lump sum	200 .-	400 .-
Mechanical excavation fees	m^3	15 .-	45 .-
Transport and disposal of excavated material	m^3	50 .-	70 .-
Trench securing	Lump sum	300 .-	600 .-

Table 5: Site Installation and Excavation Rates (*Ofri*) [100]

The estimation of labor costs for pipe installation is based on standardized reference values provided by *TheProjectEstimate.com*[101]. According to the authors, "the data were gathered through project cost, canvassed through suppliers, and through study of manuals, booklets and experiences", ensuring a practical and field-representative basis for estimating man-hours in piping work.

The table below presents a subset of these reference values, detailing the estimated number of man-hours required for each task as a function of pipe diameter. The values are given per unit (meter, piece, or connection) for the following installation operations: pipe laying and handling, attaching screw flanges, welding of flanges, welding of pipe connections, and pipe threading.

Diameter [mm]	Laying [h/m]	Flange Attach. [h/piece]	Flange Weld. [h/piece]	Conn. Weld. [h/conn]	Threading [h/conn]
150	0.97	2.21	4.10	2.10	0.74
200	1.18	2.63	5.67	2.73	1.02
250	1.50	3.26	7.14	3.26	1.45
300	1.80	3.89	8.72	3.78	1.61
350	2.21	4.73	10.50	4.52	2.18

Table 6: Reference man-hours per task as a function of pipe diameter (*TheProjectEstimate.com*) [101].

This breakdown allows for the total labor time to be computed from simple geometric and design parameters such as total pipe length, number of flanged joints, welded connections, and threadable ends. In the present study, only the tasks relevant to the configuration of the underground pipe system will be considered.
The total budget for Design 1 is thus the sum of the production and installation estimates. The installation component itself includes both the labor cost and the service-related expenses (e.g., excavation, trench securing, transport). The full expression becomes:

$$\text{Budget}_{\text{D1}} \;=\; \text{Cost}_{\text{production}} \;+\; \text{Cost}_{\text{services}} + \text{Cost}_{\text{labor}}.$$

In this formulation, $\text{Cost}_{\text{labor}}$ is derived from standardized man-hour values associated with pipe installation tasks (see Table 6), multiplied by the applicable hourly labor rate, while $\text{Cost}_{\text{services}}$ encompasses fixed and unit-based fees such as site setup, excavation, and disposal, as listed in Table 5.

3.3 Design 2 : Sensor Zone

In Design 2, illustrated on figure 14, the principal objective is to characterize the chemical state of the exhaust plume at a specified region downstream of the nozzle to capture the dynamical interactions between launcher emission and ambient atmosphere.

The first critical sizing parameter for the Sensor Zone concerns structural and thermal survivability under the high-velocity, high-temperature exhaust flow. Aerodynamic loading on the sensor housing is directly proportional to both the frontal area and the velocity squared (at area's position), necessitating a robust design and selection of materials with adequate yield strength. Thermal stresses arising from hot combustion products further require either active cooling or high-temperature alloys/coatings to prevent deformation or material degradation over the operational duty cycle. Thus, the aerodynamic force field and thermal flux become primary drivers in the mechanical design of the Sensor Zone enclosure.

The second sizing variable is the spectral requirements imposed by the target gas species. Since Design 2 integrates both sensors and imaging system, it is imperative to define the wavelength bands over which each molecular can be detected by their absorption. Utilizing the exhaust composition data tabulated in Table 2, one may extract the principal absorption bands for each species of interest (e.g., CO, CO_2, NO_x, H_2O), thereby determining the necessary bandwidth coverage for infrared and ultraviolet detectors. This information gives information about the optical design such as the required filter selection.

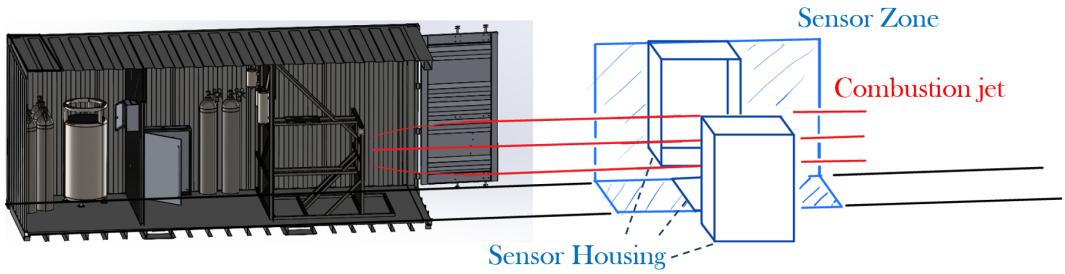

Figure 14: Illustration of the second system design

3.3.1 Gaz Species Spectral Analysis

As noted in the previous section, the usage of optical sensors and imaging systems requires an examination of the absorption bands of all species expected within the measurement volume. Accurate calibration of radiometric or spectroscopic instruments help to know which molecule will attenuate or emit radiation in the wavelengths of interest. Based on the species mole fractions predicted by the Rocket Propulsion Analysis (RPA) simulation (Table 2), we identify the principal absorbing molecules in the exhaust plume and compile their characteristic absorption bands. By summing the individual contributions, one can define the total spectral window that must be accounted for during sensor design and data interpretation.

Figure 15 summarizes the literature values of the absorption band of the dominant combustion products (H_2O, CO, CO_2, H_2, and O_2). Water vapor (H_2O) exhibits strong rotational-vibrational bands in the [1000-1400] cm^{-1} range, while carbon monoxide (CO) and carbon dioxide (CO_2) present sharp lines for ranges [2100-2300] cm^{-1} and [2300-2400] cm^{-1}, respectively. Molecular hydrogen (H_2) and oxygen (O_2) absorb weakly in the near-infrared, with bands around 4200 cm^{-1} and 1550 cm^{-1}. It also has been noted[102] that compounds featuring the OH functional group exhibit pronounced infrared absorption bands centered near 3500 cm^{-1}.

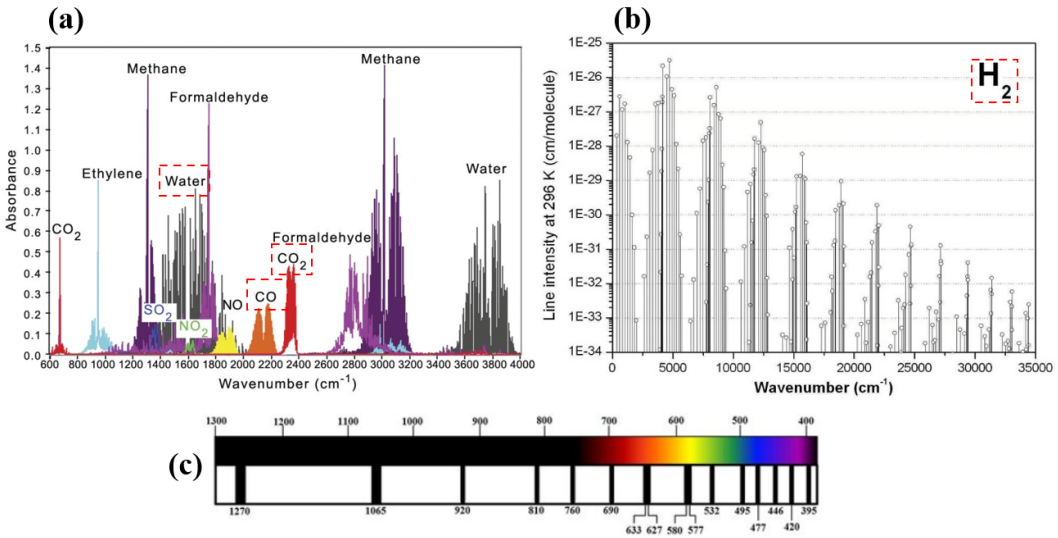

Figure 15: Reference infrared absorption data for exhaust-gas species from Table 2. **(a)** Broadband absorbance spectra of H_2O, CO, and CO_2 in the mid-IR region (600-4000 cm^{-1}) [103]. **(b)** Line intensities of H_2 at 296 K [104]. **(c)** O_2 absorption bands [105].

Based on the reviewed literature data, the frequency bands requiring coverage for sensor calibration can be anticipated. By narrowing the spectral window of interest, the demand for specialized instrumentation is reduced, thereby simplifying both procurement and experimental assembly. Consequently, the absorption band selected for each target molecule is chosen to lie as close as possible to those of the others. Using the bands compiled in Table 7, we therefore define a wavenumber range of $\lambda \in [1270, 5000]$ cm^{-1} (equivalently, a wavelength range of $\nu \in [2, 7.87]$ μm), which would be suited for the detection of H_2O, CO, CO_2, H_2, OH and O_2.

Species	λ [cm^{-1}]	ν [μm]
H_2	5000	2
OH	3500	2.86
CO_2	[2300-2400]	[4.34-4.17]
CO	[2100-2200]	[4.76-4.54]
H_2O	[1400-1800]	[7.14-5.55]
O_2	1270	7.87

Table 7: Principal infrared absorption bands for exhaust-gas species

3.3.2 Structural and Thermal Analysis

In the structural and thermal analysis of the sensor housing placed within the exhaust stream, a characterization of the local temperature and flow-velocity fields is required in order to assess both thermal loads and aerodynamic forces acting on the enclosure. Elevated temperatures can degrade sensor performance or even damage sensitive electronic components. Strong aerodynamic forces may compromise the fixed positioning of the measurement system. Consequently, we must quantify the fields of temperature T and axial velocity U in the surrounding of the combustion jet and subsequently evaluate the resulting temperature and pressure-induced stresses on the sensor housing.

To obtain these fields, we rely on the two-dimensional CFD simulations[71] presented on figure 5. Under the assumption of horizontal symmetry about the jet axis, the local conditions at a given depth z are equivalent to those at the corresponding height y. Thus, for any axial position x, we have that $T(z) = T(y)$, $U(z) = U(y)$ where $T(y)$ and $U(y)$ are the temperature and velocity profiles extracted from the 2D plane at height y.

The 3D plot (Fig. 6) of $U(x, y)$ and $T(x, y)$ shows that the height $y_{\mathrm{SC}}(x)$ at which the temperature and velocity reach the standard conditions (SC) (defined here as $U_{\mathrm{SC}} = 0\,\mathrm{m/s}$ and $T_{\mathrm{SC}} = 277\,\mathrm{K}$) increases almost linearly with x. By considering the symmetry hypothesis, we set the corresponding depth of the standard-condition equal to the height (i.e., $z_{\mathrm{SC}}(x) = y_{\mathrm{SC}}(x)$).

Figure 16 presents the isocontour of $U = U_{\mathrm{SC}} = 0$ m/s and $T = T_{\mathrm{SC}} = 277$ K in the x-y plane. These level curves define the region outside of which sensor mounting structures will be subjected to mild thermal loads and negligible aerodynamic forces.

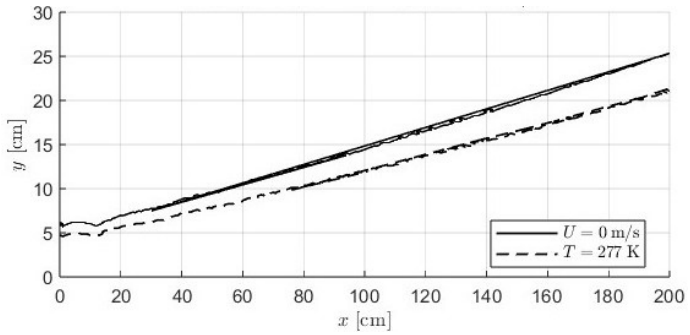

Figure 16: Level curves of the velocity and temperature at standard condition ($U_{\mathrm{SC}} = 0$ m/s, $T_{\mathrm{SC}} = 277$ K).

Thus, for each axial location x of the measurement devices, the corresponding safe depth $z_{\mathrm{SC}}(x)$ is defined. However, it must be noted that in real-world conditions this symmetry assumption is broken by ground-boundary effects: wall-induced shear leads to accelerated radial flow, yielding level-curve depths higher than those predicted by the idealized symmetric model $\left(z_{\mathrm{SC}} > y_{\mathrm{SC}}\right)$. Consequently, a safety factor should be incorporated when specifying the sensor-housing depth. Moreover, it should be noted that these level curves are obtained from CFD contours, and their accuracy is directly related to the modeling fidelity (e.g. turbulences, mesh resolution) of the underlying simulation. Therefore, validation with experimental or higher-fidelity numerical data is recommended to ensure the reliability of the defined safe-zone boundaries.

3.3.3 Budget 2

Given that Design 2 consists solely of measurement devices positioned at a secure location within the exhaust zone, the primary costs associated with its implementation are related to the acquisition of the required instrumentation.

As detailed in the spectral analysis of exhaust gases (Section3.3.1), the imaging devices must jointly cover the full infrared absorption range of the target species, which spans from 2 to 7.87μm. To achieve this, two infrared cameras are employed: Camera 1, covering the [1.5–5]μm range, and Camera 2, covering the [5.5–11]μm range. Based on the absorption characteristics of the species, Camera 1 is used to detect CO_2, CO, H_2, and OH, while Camera 2 is dedicated to the detection of H_2O and O_2.

In addition to the instrumentation costs, minor expenditures related to the housing of the measurement devices must also be considered. As discussed in the thermal and structural assessment (Section 3.3.2), the sensors are positioned at a sufficient distance from the nozzle exit such that the flow conditions approach ambient standards ($U = 0$ m/s and $T = 277$ K). Consequently, both the devices and their enclosures are subject to negligible thermal and mechanical constraints. This allows for a cost-effective solution where standard enclosed industrial shelving, preferably constructed from aluminum, can be used to house the equipment. Given their simplicity and commercial availability, these enclosures represent a minor fraction of the overall budget for Design 2.

The total budget for Design 2 can be expressed as the sum of the instrumentation, housing, and

auxiliary system costs:

$$\text{Budget}_{\text{D2}} = \text{Cost}_{\text{devices}} + \text{Cost}_{\text{housing}} + \text{Cost}_{\text{integration}}.$$

In this formulation, $\text{Cost}_{\text{devices}}$ refers to the acquisition cost of the infrared cameras and spectral filters required to detect the relevant exhaust-gas species across the absorption bands listed in Table 7. The term $\text{Cost}_{\text{housing}}$ accounts for the physical enclosures supporting the measurement devices. As detailed in Section 3.3.2, the sensors are located in a region where the flow conditions approximate ambient values ($U = 0$ m/s and $T = 277$ K), allowing for low-cost structural solutions such as closed aluminum shelving. Finally, $\text{Cost}_{\text{integration}}$ encompasses additional expenses associated with system operation and connectivity, including cabling, power delivery, signal acquisition hardware, data processing units, and remote communication links with the control station. These auxiliary costs ensure the seamless integration of the measurement system into the test infrastructure.

3.4 Design Assessment

The evaluation of the two measurement systems must begin by acknowledging their fundamentally different observational intents. Design 1 is conceived to extract and analyze a sample of the exhaust gases directly from the combustion jet. Its purpose is to obtain a chemically undisturbed representation of the emitted mixture, allowing for precise quantification of individual species concentrations at the nozzle exit. This approach prioritizes the characterization of the gas as it is generated, with minimal influence from ambient conditions.

In contrast, Design 2 is built around the observation of the interaction between the exhaust plume and the surrounding atmosphere. By using infrared imaging systems placed at a safe distance from the jet, this method provides spatially and spectrally resolved information about how exhaust gases diffuse, dilute, and potentially react with ambient air. Rather than isolating the exhaust in its purest form, Design 2 captures its dynamic evolution post-release.

These differences imply that the two systems serve distinct, yet complementary scientific purposes. As such, any performance comparison must take into account not only technical and economic criteria, but also the relevance of each system to the experimental objectives. The methodology proposed in this project proceeds as follows: each design is assessed across five distinct dimensions, each comprising several binary criteria designed to be ideally answered with either 'yes' (1/1) or 'no' (0/1) (Section 3.5.1 to 3.5.5). The mean value of these binary criteria defines the overall score for each assessment dimension. Subsequently, by applying a weighting scheme to these dimensions, which dependent on the specific experimental context within one of the two designs is intended to be implemented,it is possible to objectively determine the optimal design to prioritize.

3.4.1 Integration to Test Bench

This criterion assesses the degree of complexity associated with integrating each measurement system into an existing horizontal propulsion test bench. It is intended to provide a practical basis for comparing the two designs in terms of implementation effort, with the goal of estimating which system requires the least disruption to current infrastructure and operational routines. Ultimately, this metric informs the timeline required for system deployment and contributes to the overall feasibility assessment.

The first dimension of this criterion concerns whether the system requires physical modification of the test bench itself. If any alteration of the original setup is necessary, such as excavation, structural changes, or tapping into existing resource networks,the system is assigned a score of 0 out of 1. If the system can be implemented without altering the base infrastructure, it receives a score of 1 out of 1. In this regard, Design 1 present non-negligible intervention: it requires excavation of the initial ground to lay piping for exhaust gas transport and the adding of an additional device (i.e. the counter-flow cooling system) that draws nitrogen from the existing base stock. Therefore, it is assigned a score of 0/1. By contrast, Design 2 involves only the addition of imaging equipment positioned around the exhaust zone and electronical connections to the control station, without any impact on the test benchs physical structure or fluid networks. Design 2 is thus assigned a score of 1/1.

The second dimension concerns the need for external professional services during implementation. If the installation demands expertise or tools beyond those available within the EPFL Rocket Team, such as industrial excavation equipment or certified operators, the system receives a score of 0 out of 1. If the system can be fully deployed using internal resources, it is scored 1 out of 1. Because Design 1 requires excavation and installation of buried piping, its realization depends on external contractors and industrial capabilities, warranting a 0/1 score. Design 2, on the other hand, can be installed entirely by the Rocket Team, using standard mechanical and electrical integration techniques, and is therefore assigned a score of 1/1.

A third dimension examines whether the measurement systems interfere with the primary measurands of the original test bench. If any of the proposed systems alters or disturbs the key quantities being measured, such as thrust, flow rate, or temperature, then a score of 0/1 is assigned. Otherwise, the system is scored 1/1. In the present case, the main objective of the FireHorn I propulsion test bench is to measure the engine's thrust. Neither Design 1 nor Design 2 interferes with this measurement. Design 1 samples a small fraction of the exhaust gases downstream of the nozzle and the shockwave, while Design 2 performs optical measurements outside the core flow. Accordingly, both systems are assigned a score of 1/1. A summary of the scores regarding this criterion is summarized on table 8 :

Integration to Test Bench	**Observation**	**Design 1**	**Design 2**
Intervention on Initial Test Bench	Excavation, Piping re-networking (Design 1)	0/1	1/1
External Professional Services	Heavy Equipment, Technical expertise (Design 1)	0/1	1/1
Interference with Primary Measurands	No impact on thrust measurement for either system	1/1	1/1
Total		**1/3**	**3/3**

Table 8: Scoring of the integration complexity for each design

3.4.2 Robustness Against Environment

This criterion evaluates the extent to which the performance of each measurement system is dependent on environmental conditions. A robust system is expected to operate reliably and reproducibly across a range of ambient scenarios without requiring strict control of its surroundings. The assessment focuses on two primary environmental variables: ambient light level and atmospheric humidity. The first variable considered is the level of ambient light. If the measurand of the system is influenced by variations in lighting conditions, the system is assigned a score of 0 out of 1. Otherwise, it receives a score of 1 out of 1. Design 2, which relies on infrared optical imaging, is inherently sensitive to external illumination. Ambient light, especially solar radiation, can interfere with the optical signal-to-noise ratio and limit detection accuracy. As a result, the system is unsuitable for nocturnal tests and must operate under daylight conditions. It is thus scored 0/1. In contrast, Design 1 is based on the physical extraction and transport of exhaust gas through conduits toward a separate analysis unit. This process is entirely independent of ambient light levels, earning it a score of 1/1.

The second variable is ambient humidity. Here again, if the measurand is affected by the humidity level in the surrounding air, the system receives a score of 0 out of 1. Otherwise, it scores 1/1. In the case of Design 2, the target of observation is the interaction between the exhaust plume and the ambient atmosphere. This interaction is sensitive to the preexisting humidity, which may alter mixing dynamics and radiative signatures. Consequently, the system receives a score of 0/1. For Design 1, the sampled exhaust gas is isolated shortly after its emission, and the brief transport to the collection vessel is generally unaffected by external moisture unless extreme weather conditions occur (e.g., heavy rainfall). The effect of ambient humidity is therefore negligible, and the system is assigned a score of 1/1.

A third environmental variable concerns the susceptibility of each system to wind disturbances. If wind conditions are likely to compromise the performance or integrity of the setup, the system receives a score of 0/1. Otherwise, it is scored 1/1. Design 1 is built to operate within the high-velocity core of the exhaust plume, where jet velocities reach up to $U = 2000$ m/s. It is thus assigned a score of 1/1. While Design 2 involves externally mounted optical instruments that could in principle be disturbed by strong winds, the associated housing structures are intended to ensure stability under typical weather conditions. Although extreme wind events may pose a risk, the system remains operational in all standard testing scenarios. Therefore, a score of 0.5/1 is attributed to Design 2.

Finally, both systems are evaluated with respect to their tolerance to ambient temperature variations. We consider that the ambient temperatures may range from $T_{\text{amb}} = -20°\text{C}$ to 60°C. These values are well within the operating range of the components in both systems. Design 1 handles gas temperatures exceeding 2000 K, while most commercial hyperspectral infrared cameras used in Design 2 are rated for continuous operation up to 300 °C and below freezing conditions. Consequently, both systems are deemed robust against thermal environmental variations and receive a score of 1/1.

Robustness Against Environment	**Observation**	**Design 1**	**Design 2**
Sensitivity to Ambient Light	Light-dependent optical detection; restricted to daytime use (Design 2)	1/1	0/1
Sensitivity to Humidity	Interaction with ambient air affected by humidity (Design 2)	1/1	0/1
Sensitivity to Wind	Design 2 protected by housing under standard wind conditions, but may be comprised for extreme condition	1/1	0.5/1
Sensitivity to Ambient Temperature	Components rated well beyond typical ambient ranges in both designs	1/1	1/1
Total		**4/4**	**1.5/4**

Table 9: Scoring of the environmental robustness for each design

3.4.3 Operational Complexity

This criterion evaluates the practical complexity of operating each measurement system. It reflects the level of technical expertise required to obtain the desired measurand, as well as the operational autonomy of the system during test execution. In this context, the assessment focuses on three aspects: in-test intervention, required personnel, and system calibration.

The first dimension addresses whether an intervention is needed during the propulsion test itself. If the system requires manual or active adjustment during the firing sequence, it receives a score of 0 out of 1. Otherwise, it is scored 1 out of 1. In the case of Design 1, only a portion of the exhaust gas is intended to be collected during the test, which implies the need to actuate a valve in real time to control the quantity of gas stored in the sealed receptacle. This necessitates some form of synchronization or supervision during the test and justifies a score of 0/1. By contrast, Design 2 involves imaging systems that can be triggered before or after the test begins and require no interaction while the motor is firing. As a result, it receives a score of 1/1.

The second dimension concerns the personnel required to obtain the targeted measurand. If data acquisition or analysis depends on experts external to the EPFL Rocket Team, a score of 0 out of 1 is assigned. If the entire process can be handled by internal team members, the system receives a score of 1/1. For Design 1, the gas collected must be analyzed by a specialized external laboratory equipped to perform chemical composition analysis, which introduces dependence on external expertise. This results in a score of 0/1. In contrast, Design 2 involves the use of infrared imaging and associated data processing techniques that are within the scope of bachelor and master level competencies in the team. The full operational pipeline, from data acquisition to spectral analysis, can be managed internally, earning it a score of 1/1.

The third dimension relates to the systems need for calibration prior to testing. If the system requires complex or test-specific calibration, it receives a lower score. In this case, both systems involve some degree of pre-test setup, but not to the same extent. For Design 1, calibration primarily consists of determining the optimal opening time of the sampling valve and the axial positioning of the probe. These adjustments are generally constant across tests of the same propulsion configuration and do not require frequent repetition. Once defined for a given engine type, they remain valid across multiple test runs, making calibration relatively lightweight. For this reason, Design 1 is assigned a partial score of 0.5/1. By contrast, Design 2 involves optical detection systems that are directly affected by varying environmental conditions, including humidity, ambient light, and wind-induced turbulence. These factors can fluctuate from one test to another, requiring frequent re-calibration of both hardware and signal processing parameters to ensure measurement reliability. The dynamic nature of these calibrations justifies a score of 0/1 for Design 2.

Operational Complexity	**Observation**	**Design 1**	**Design 2**
In-Test Intervention	Manual valve actuation required during firing (Design 1); fully autonomous operation in Design 2	0/1	1/1
Required Personnel	External gas analysis laboratory needed for Design 1; image processing handled internally (Design 2)	0/1	1/1
Calibration Requirements	Design 1 requires one-time calibration per engine; Design 2 requires re-calibration for each test due to environmental variability	0.5/1	0/1
Total		**0.5/3**	**2/3**

Table 10: Scoring of operational complexity for each design

3.4.4 Overall Feasibility

This criterion evaluates the fundamental realizability of each measurement system as a standalone concept, independent of its integration or performance. It reflects the degree to which each design can be implemented with standard resources, without requiring significant industrial processing. Two key aspects are considered: budgetary feasibility and the need for pre-processing or industrial modification.

The first dimension evaluates the estimated budget required for each system. Design1, which involves heavy infrastructure such as piping, flow control devices, heat exchangers, and field integration, results in a total estimated cost of over 40 000 $. This substantial investment, driven by the use of refractory metals and labor-intensive installation, justifies a score of 0/1. Design 2, although structurally simpler, results in an even higher cost due to the use of hyperspectral infrared cameras, each ranging from 65,000 to 170,000 $. However, since this cost stems from the chosen technology rather than the design itself, and more affordable alternatives could be considered, Design 2 is assigned a moderated score of 0.5/1 to reflect both its current expense and its potential for cost reduction.

The second dimension evaluates whether the system requires industrial pre-processing prior to deployment. If components must be machined, welded, or modified using professional equipment, the design is given a score of 0/1. Although the elements of Design 1 are commercially available, adapting the system to a different rocket configuration may require dimensional adjustments (e.g., turning or welding of metal piping) as well as surface treatment to control flow properties. These steps necessitate industrial expertise and specialized equipment. Therefore, Design 1 receives a score of 0.5/1. Design 2, in contrast, is composed of optical instruments that are ready to use upon delivery. No additional mechanical processing is needed, and the system can be assembled and calibrated directly by the Rocket Team. For this reason, Design 2 receives a score of 1/1.

The third dimension considers the availability of materials and components required for each system. If a system relies on rare or difficult-to-source elements, it receives a score of 0 out of 1. Otherwise, it is assigned a score of 1/1. According to Table 3, the potential materials for the conduits in Design 1 include both rare and costly options, as well as more accessible alternatives such as tungsten and chromium. These are widely available on the commercial market, justifying a score of 1/1. Similarly, the spectral range required for Design 2 ($\nu \in [2,\ 8.3]\ \mu$m) falls well within the operating range of standard infrared imaging systems. The components for this system are thus readily available, and Design 2 also receives a score of 1/1.

Overall Feasibility	**Observation**	**Design 1**	**Design 2**
Budget Requirements	Design 1 involves piping, storage, and gas redirection infrastructure; Design 2 uses compact optical devices	0/1	0.5/1
Pre-processing / Industrial Modification	Design 1 may require machining, welding, and surface treatment; Design 2 uses ready-to-operate commercial devices	0.5/1	1/1
Component Availability	Design 1 uses accessible industrial materials (e.g., tungsten, chromium); Design 2 relies on standard infrared imaging components	1/1	1/1
Total		**1.5/3**	**2.5/3**

Table 11: Scoring of feasibility for each design

3.4.5 Adaptability

This criterion evaluates the capacity of each measurement system to be adapted to alternative experimental contexts. Beyond the immediate scope of the FireHorn I test bench, a highly adaptable system can serve as a basis for future studies in different propulsion regimes, configurations, or scientific domains.

The first dimension concerns the systems ability to be implemented on a mobile platform. If a measurement setup can reasonably be integrated into a moving system, it is assigned a score of 1 out of 1. Design 1, although requiring significant redesign, could theoretically be implemented in such a context. In particular, the gas sampling system would need to be re-engineered using compact alternatives to the current counter-flow configuration, such as shell-and-tube heat exchangers, and the storage solution would require robust pressurization and miniaturization strategies, justifying a score of 0.5/1. In contrast, Design 2 relies on fixed-position optical measurements taken at a radial distance z_{SC} from the exhaust axis. Transposing this configuration to a mobile system would present major mechanical and optical challenges. Housing and camera alignment would require additional structural supports that are difficult to implement in dynamic environments, and such integration would demand extensive engineering development. Also, since Design 2 focuses on the interaction of the exhaust gaz with the surrounding ambient air, its integration into a mobile device affects the purpose of the design. Therefore, Design 2 is scored 0/1.

The second dimension evaluates the capacity of each system to accommodate different thrust levels in horizontal testing. A system that can be easily rescaled to accommodate higher exhaust velocities and gas volumes receives a score of 1 out of 1. For Design 1, increasing the propulsion level would necessitate redesigning the entire sampling and transfer architecture, potentially pushing the system into an economically or mechanically unfeasible regime. However, the chemical composition of larger thrusters could still be investigated using downscaled analogs, preserving the validity of the measurement objective. This partial adaptability justifies a score of 0.5/1. For Design 2, a higher thrust level would mainly result in an increase in the radial distance required between the exhaust core and the imaging devices. This may call for a wider optical field of view but would not compromise the systems feasibility. Accordingly, Design 2 is scored 1/1.

The third dimension concerns the adaptability of each system to vertical test bench configurations. If the design can be used in a vertical orientation without major reengineering, it is assigned a score of 1/1. For Design 1, such a configuration would require considerable modification of the sampling and redirection system. In particular, the orientation of the conduits may imply a substantial redesign, though not a fundamental incompatibility. Design 1 is therefore assigned a score of 0.5/1. For Design 2, while the optical configuration is generally indifferent to jet orientation, the dynamics of a vertical exhaust flow differ significantly from the horizontal case. This change may influence the structure of the plume and the spatial evolution of the absorption zones. As a result, the optimal measurement radius z_{SC} may need to be reevaluated through new flow simulations or experimental calibration. However, these adjustments do not require hardware redesign, and the system remains broadly compatible with vertical setups. Design 2 thus retains a score of 1/1.

Adaptability	**Observation**	**Design 1**	**Design 2**
Adaptability to Mobile Systems	Design 1 theoretically adaptable with significant redesign; Design 2 incompatible	0.5/1	0/1
Adaptability to Higher Thrust Testing	Design 1 valid for scaled models but with limit	0.5/1	1/1
Adaptability to Vertical Test Benches	Design 1 requires conduit reconfiguration	0.5/1	1/1
Total		**1.5/3**	**2/3**

Table 12: Scoring of adaptability for each design based on mobility, scalability, and orientation.

3.4.6 Weighting Scheme

This section establishes three distinct experimental contexts, each characterized by a different weighting of the five assessment dimensions. By assigning specific weighting coefficients to each dimension, the suitability of each measurement design under varying contexts can be objectively evaluated. The weighting coefficients are defined as follows: a dimension considered negligible or indifferent within a given context is assigned a coefficient of 0.5, a neutral dimension (neither negligible nor highly critical) receives a coefficient of 1, while an important dimension, ideally to be optimized, is allocated a coefficient of 1.5.

Initially, a baseline scenario is considered without a specific context. In this scenario, all assessment dimensions are treated equally, implying that each dimension is equally important. Consequently, each dimension is uniformly assigned a coefficient of 1.

The second context is the EuRoC competition, in which the EPFL Rocket Team participates. Two primary constraints emerge in this scenario: budgetary limitations and time availability, typical of student-led projects. Thus, the primary requirement is for the measurement system to be quickly and easily integrated into the existing propulsion test bench to limit budget consumption and avoid the necessity for an additional specialized test bench dedicated solely to emissions measurements. Hence, the dimension "Integration to Test Bench" is assigned a coefficient of 1.5. Similarly, driven by budgetary constraints, the dimension "Overall Feasibility," reflecting the need to minimize the number of industrial processes involved, also receives a weighting of 1.5. The "Operational Complexity" of the system should be moderate: although the system may require engineering knowledge (as it will be operated by engineering students), it must not necessitate professional-level expertise. Therefore, this dimension is allocated a neutral coefficient of 1. Because the measurement system will be used only within the limited scope of the competition, there is no need to further develop its adaptability for other applications, resulting in a weighting of 0.5 for the "Adaptability" dimension. Finally, the test site selected for this competition typically experiences standard meteorological conditions, thus justifying a lower priority assigned to "Robustness Against Environment," also receiving a coefficient of 0.5.

The third context is an academic research setting, characterized by higher budgets, broader technical and scientific expertise, and more flexible deadlines. In this context, priorities shift significantly. Because precise, detailed measurements are desired and adequate funding is available, ease of integration into a pre-existing test bench is no longer a critical factor. Consequently, the dimension "Integration to Test Bench" is assigned a coefficient of 0.5. For similar reasons, feasibility concerns are reduced, as complex and even challenging experimental setups are commonly pursued in scientific research; thus, "Overall Feasibility" also receives a coefficient of 0.5. Moreover, given that research is typically conducted by professional technicians and scientific staff, the importance of "Operational Complexity" is reduced, justifying another weighting of 0.5. On the other hand, if the measurement system is intended for deployment at multiple launch sites with varying temperature extremes, the dimension "Robustness Against Environment" becomes a high priority, receiving a coefficient of 1.5. Finally, the "Adaptability" dimension receives a neutral weighting coefficient of 1, although it is noted that in a commercial context this dimension could reasonably warrant a higher weighting of 1.5. Table 13 displays a summary of the weighting factors for each context.

	Weighting Factors		
Dimension	**No Context**	**EuRoC**	**Research**
Integration to Test Bench	1	1.5	0.5
Robustness Against Environment	1	0.5	1.5
Operational Complexity	1	1	0.5
Overall Feasibility	1	1.5	0.5
Adaptability	1	0.5	1

Table 13: Weighting factors assigned to each assessment dimension across the three experimental contexts.

4 Results

4.1 Summary of Design 1 Characteristics

Figure 17 shows a CAD model of Design 1.

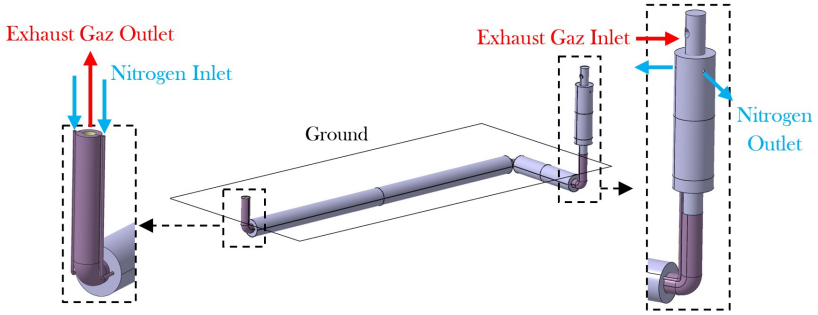

Figure 17: CAD model of the Design 1 pipe assembly, showing the exhaust gas and nitrogen cooling circuits.

Table 14 summarizes the structural constraints to which the sampling probe is subjected to, for a configuration in which the probe is 1.60 meters long and positioned 60 cm from the exhaust outlet. These values are based on previously established CFD simulation results of the exhaust gas flow.

Parameter	**Value**
Sampling Probe Position [m]	0.60
Sampling Probe Height [m]	1.60
Impact Velocity [m/s]	2000.00
Impact Temperature [K]	2500.00
Max Drag Force [N]	27 648.00
Max Distributed Load [N/m]	17 280.00

Table 14: Summary of structural and thermal conditions applied to the sampling probe in Design 1.

Figure 18 shows, on the left, the maximum stresses induced by aerodynamic forces on the sampling probe, alongside the yield strengths and melting temperatures of the materials listed in Table 3, as computed through structural numerical simulations. On the right, Figure 18 illustrates the structural safety margins with respect to the elastic limit and the phase change threshold, assuming a probe temperature of $T = 2500$ K.

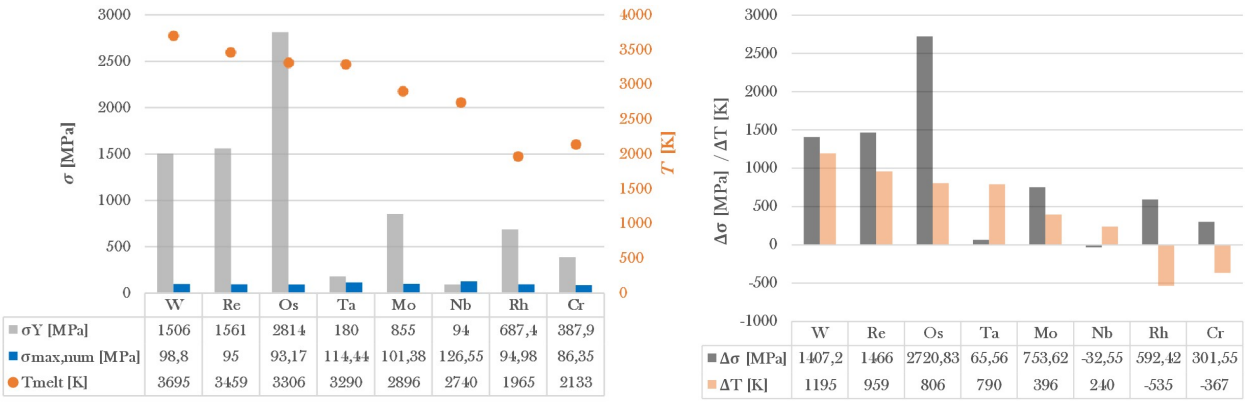

Figure 18: Comparison of structural and thermal margins for each material: (left) Yield strength versus simulated stress with melting temperatures; (right) Safety margins $\Delta\sigma = \sigma_Y - \sigma_{\max}$ and $\Delta T = T_{\text{melt}} - 2500$.

Figure 18 reveals that several materials fail to meet the thermal or mechanical constraints imposed on the sampling probe. Specifically, Rhodium (Rh) and Chromium (Cr) exhibit negative temperature margins of $\Delta T_{\text{Rh}} = -535$ K and $\Delta T_{\text{Cr}} = -367$K, respectively, with respect to the operational probe temperature of 2500 K. This indicates that these materials would reach their melting point and undergo phase change under these conditions. Consequently, they are excluded from further consideration.

From a mechanical perspective, Niobium (Nb) demonstrates insufficient strength to withstand the aerodynamic loading caused by the combustion jet. A negative margin of $\Delta\sigma_{\text{Nb}} = -32.55$ MPa indicates that the material would yield under stress, making it unsuitable for this application. Similarly, Tantalum (Ta), although not plastified, exhibits a low safety margin of $\Delta\sigma_{\text{Ta}} = 65.56$ MPa. Considering its relatively high price of $P_{\text{Ta}} = 305$ \$/kg, the material is considered structurally underperforming for its cost and is thus excluded from budgetary calculations.

From a financial standpoint, Rhenium (Re) and Osmium (Os) are also dismissed due to their prohibitive costs of, respectively, $P_{\text{Re}} = 3\ 580$ \$/kg and $P_{\text{Os}} = 1\ 922\ 040$ \$/kg, placing them well beyond the range of typical student project budgets. As a result, the final cost estimation will be carried out using the two viable candidates that satisfy both thermal and mechanical requirements while remaining financially accessible: Tungsten (W) and Molybdenum (Mo).

Table 15 presents the thermal characteristics of the counter-flow heat exchanger, using pure tungsten for the gaz conduction pipe material and nitrogen at 100K as the cooling fluid, aimed at reducing the exhaust gas temperature to an outlet value of 1200K. This cooling process is performed to prevent the occurrence of unwanted chain reactions that could be triggered by excessively high post-combustion temperatures.

Parameter	**Value**
Heat Exchanger Type	Counter-Flow
Outer Diameter [m]	0.320
Inner Diameter [m]	0.240
Wall Thickness [m]	0.040
Cooling Medium	Nitrogen (N_2)
Inlet Gas Temperature [K]	2500.00
Outlet Gas Temperature [K]	1200.00
Inlet Nitrogen Temperature [K]	100.00
Outlet Nitrogen Temperature [K]	671.96
Gas Convective Coefficient [W/m^{2}K]	1212.60
Nitrogen Convective Coefficient [W/m^{2}K]	682.23
Total Length [m]	14.00

Table 15: Summary of thermal and convective characteristics of the counter-flow heat exchanger.

Table 16 presents the characteristics related to the conduction of exhaust gas, considering that the conduction pipe is made of pure tungsten with an average surface roughness of 11.35 μm. The analysis of pressure losses along the pipe highlights the need for an external flow control device at the outlet to regulate the exhaust discharge rate and ensure consistent operating conditions.

Parameter	Value
Inlet Velocity [m/s]	2000.00
90° Elbow Loss Factor [-]	0.30
Average Surface Roughness [μm]	11.35
Pressure Loss [MPa]	162.00
Friction Loss [Pa]	4.40
Outlet Velocity [m/s]	1923.30

Table 16: Summary of flow conduction results for the exhaust gas through the pipeline.

4.1.1 Budget 1

The production cost of the system is estimated based on the material requirements listed in Table 17, which summarizes the dimensions and volumes of each component in Design 1. The conduction pipe and the sampling probe, being directly exposed to the high-temperature and high-stress environment of the exhaust plume, must be fabricated using high-performance refractory metals. As previously determined, the two viable candidates are tungsten and molybdenum. Consequently, an average price per kilogram is computed by taking the mean between the prices of both metals listed in Table 3. In contrast, the counter-flow heat exchanger, which is buried underground and therefore not subjected to the same mechanical or thermal constraints, can be made from conventional structural steel. For this component, standard iron is assumed, with a density of $\rho_{\text{Fe}} = 7874$ kg/m^3 and a market price of $P_{\text{Fe}} = 0.42$ \$/kg[106]. This simplification is justified by the exchangers installation context, which protects it from elevated temperatures and aerodynamic loads. By applying the individual material prices to the respective volumes and densities of each component, and summing the results, the total estimated material cost amounts to $\text{Cost}_{\text{Production}} = 42\,032.45$ \$.

	Pipe		**Heat Exchanger**
Total Length [m]	15.271		14.000
Internal Dia. [m]	0.080		0.240
External Dia. [m]	0.160		0.320
Cross-Section [m^2]	0.005		0.005
Total Volume [m^3]	0.077		0.070
Number of Connection [conn.]	3		2
Total Mass [kg]	Tungst.	Molybd.	Fe
	1 478.713	782.956	554.107
Part Cost [$]	52 198.558	31 396.55	234.9
Average Part Cost [$]	41 797.55		234.9
Average Material Cost [$]			**42 032.45**

Table 17: Summary of component dimensions, material mass, and associated production costs for Design 1.

The setup cost associated with the installation of the pipe is estimated using reference values provided in Table 5, as reported by Ofri[100]. The total setup cost is calculated as the sum of the average values between the minimum and maximum unit prices for each preparatory stage of the installation process. These stages include site setup, road access preparation, mechanical excavation, material transport, and trench securing. The resulting average values for each of these services are summarized in Table 18. This yields a total estimated setup cost of $\text{Cost}_{\text{services}} = 1\,621.20$ \$.

Service	**Average Cost [$]**
Site Installation	450.00
Access road preparation	300.00
Excavation	140.40
Transport of Excavated Material	280.80
Trench Securing	450.00
Average Trench Setup Cost [$]	**1 621.20**

Table 18: Average setup cost per service stage for trench installation, based on reference estimation

The estimation of labor cost is based on the reference man-hour values provided by TheProjectEstimate.com[101], summarized in Table 6. These reference values were extrapolated to match the specific pipe diameters used in this project, resulting in the adjusted values reported in Table 19.

Diameter [mm]	**Laying [h/m]**	**Flange Attach. [h/piece]**	**Flange Weld. [h/piece]**	**Conn. Weld. [h/conn]**	**Threading [h/conn]**
160	1.01	2.29	4.41	2.23	0.80
320	1.96	4.23	9.43	4.08	1.84

Table 19: Extrapolated reference man-hours per task as a function of pipe diameter.

Using these extrapolated man-hour coefficients, the total labor time required for the installation of the piping system was computed by summing the contributions from laying, flange welding and connection welding. This provides the total number of labor hours necessary for full pipeline assembly. To estimate the labor cost, the average hourly wage of the relevant construction roles was determined based on public data obtained from *top-metiers.fr*[107]. The professions considered include pipe layers, trench workers, and piping technicians. Their respective monthly wages were used to calculate an average hourly wage, as shown in Table 20.

Position	**Monthly Salary [Euro]**	**Hourly Rate [Euro/h]**
Pipelayer	1987	10.92
Pipeline Installer	1952	10.78
Team Leader (Pipelaying)	2508	13.75
Pipeline Network Agent	2047	11.25
Pipeline Builder	2615	14.87
Average Hourly Rate		**12.20**

Table 20: Monthly and hourly wage reference for positions related to pipeline installation. [107]

Multiplying the total estimated labor hours by this average hourly rate yields the mean labor cost. As summarized in Table 21, the resulting total labor cost for the pipeline installation is calculated as $\text{Cost}_{\text{labor}} = 802.54$ \$.

	Pipe and Heat Exchanger
Laying [h]	27.496
Connection Welding [h]	8.152
Total Hours [h]	35.648
Mean Salary [Euro/h]	12.20
Average Labor Cost per Part [Euro]	434.98
Average Labor Cost per Part [$]	494.44
Average Labor Cost [$]	**494.44**

Table 21: Estimated labor costs for Design 1 realisation

Finally, the average total budget required for Desgin 1 realization is the sum of the average material cost, the average trench setup cost and the average labor cost :

$$\text{Budget}_{\text{D1}} = \text{Cost}_{\text{production}} + \text{Cost}_{\text{services}} + \text{Cost}_{\text{labor}} = 44\,148.10\ \$$$

4.2 Summary of Design 2 Characteristics

Table 22 presents the infrared absorption bands of the chemical species contained in the exhaust gas, along with the selected imaging cameras assigned for their detection. The sequence XXX corresponds to the camera's model, which varies depending on other parameters such as frame rate and calibration settings.

Formula	**Mole Fraction**	ν [μm]	**Camera**	ν_{cam} [μm]	**Price [$/cam]**
H_2	0,08700	2	FLIR XXX InSb	[1.5 – 5]	65k - 170k
OH	0,00200	2,86			
CO_2	0,20800	[4.17–4.34]			
CO	0,19100	[4.54–4.76]			
H_2O	0,50900	[5.55–7.14]	Telops FAST XXX	[5.5 – 11]	67k - 170k
O_2	0,00008	7,87			

Table 22: Spectral characteristics of exhaust species and corresponding infrared camera specifications.

Table 19 presents, for various axial positions x, the depth z_{sc} at which the sensors are expected to be exposed to standard conditions, under the assumption of a symmetric flow.

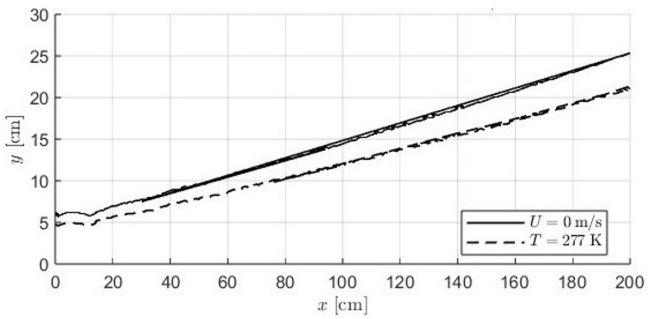

x [cm]	z_{SC} [cm]
0	5.0
20	7.0
40	9.0
60	11.0
80	13.5
100	15.0
120	17.0
140	19.0
160	21.0
180	23.0
200	25.0

Figure 19: Level curve of the temperature field at standard conditions (SC) with $U = 0$ m/s and $T = 277$ K (left), alongside the corresponding values of z_{sc} as a function of x (right), under the assumption of a symmetric flow. The listed values represent the depth z_{SC} at which the sensing devices are expected to be exposed to SC.

4.2.1 Budget 2

Technical discussions conducted with FLIR Systems and Telops Inc. led to the selection of two appropriate cameras covering distinct spectral ranges: one capable of detecting chemical species within the absorption band $\nu \in [1.5, 5]$ μm, and the other covering $\nu \in [5.5, 11]$ μm. According to the information provided by the manufacturers, both cameras fall within a similar price range, approximately 65 000 $ to 170 000 $ depending on the configuration options such as resolution, frame rate, and calibration setup (different cameras are shown in figure 23 in appendix). Assuming entry-level models for each device, we compute a mean cost of $\text{Cost}_{\text{Devices}} = 132\,000$ $.

In addition to the imaging systems, two supplementary cost components were included in the estimation: the cost of protective housing for the cameras, CostHousing, and the cost associated with integration and setup, CostIntegration. These values were estimated through preliminary research and online market surveys. Most commercially available industrial cabinets or shelving units suitable for mounting and shielding the infrared cameras were priced between 300 and 500 $. As such, a mean value of $\text{Cost}_{\text{Housing}} = 400$ $ was retained. Similarly, the cost related to basic integration, including structural supports, mounting hardware, and initial setup logistics, was approximated at a negligible average of CostIntegration = 150 $. Summing all components, the total estimated budget for the implementation of Design 2 amounts to BudgetD2 = 132 650 $.

$$\text{Budget}_{\text{D2}} = \text{Cost}_{\text{devices}} + \text{Cost}_{\text{housing}} + \text{Cost}_{\text{integration}} = 132\,650\,\$$$

4.3 Design Assessment

Table 23 provides a summary of the evaluation for each dimension and its corresponding criteria, with the total score expressed as a percentage. Figure 20 is a radar representation of table 23.

Criterion	Design 1	Design 2
1 Integration to Test Bench	**1/3 (33%)**	**3/3 (100%)**
Intervention on Initial Test Bench	0/1	1/1
External Professional Services	0/1	1/1
Interference with Primary Measurands	1/1	1/1
2 Robustness Against Environment	**4/4 (100%)**	**1.5/4 (38%)**
Sensitivity to Ambient Light	1/1	0/1
Sensitivity to Humidity	1/1	0/1
Sensitivity to Wind	1/1	0.5/1
Sensitivity to Ambient Temperature	1/1	1/1
3 Operational Complexity	**0.5/3 (17%)**	**2/3 (67%)**
In-Test Intervention	0/1	1/1
Required Personnel	0/1	1/1
Calibration Requirements	0.5/1	0/1
4 Overall Feasibility	**1.5/3 (50%)**	**2.5/3 (83%)**
Budget Requirements	0/1	0.5/1
Pre-processing / Industrial Modification	0.5/1	1/1
Component Availability	1/1	1/1
5 Adaptability	**1.5/3 (50%)**	**2/3 (66%)**
Adaptability to Mobile Systems	0.5/1	0/1
Adaptability to Higher Thrust Testing	0.5/1	1/1
Adaptability to Vertical Test Benches	0.5/1	1/1
Total Score (All Criteria)	**8.5/16 (53%)**	**11.0/16 (69%)**

Table 23: Evaluation of both measurement systems based on criteria distributed across five assessment dimensions.

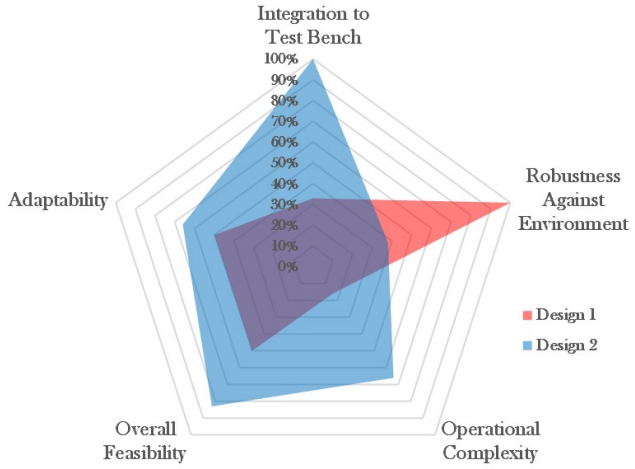

Figure 20: Comparative radar chart of Design 1 and Design 2 performance across five key evaluation dimensions

The total score for each design with weight imposed on each dimension according to table 13 is shown on table 21.

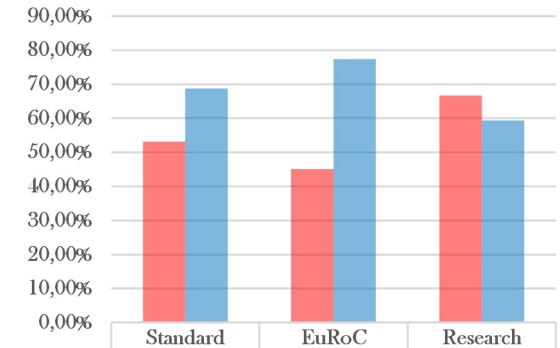

	Standard	EuRoC	Research
Design 1	53,13%	45,13%	66,67%
Design 2	68,75%	77,39%	59,33%

Figure 21: Total score with dimension multiplied by weighting factors presented on table 13

5 Analysis

5.1 Design 1

5.1.1 Critical Review on Design Methodology

The design of System 1 was guided by three major constraints: (i) the structural and thermal resistance of the sampling probe under exposure to the exhaust jet, (ii) the need to reduce gas temperature to prevent post-combustion chain reactions, and (iii) the conduction performance required to transport gas efficiently toward a sealed storage unit for subsequent laboratory analysis.

The structural analysis considered only the aerodynamic drag force F_D exerted by the combustion jet on the sampling probe. This scenario corresponds to an elementary case of flow around a cylinder, where the drag is given by $F_D = \frac{1}{2}\rho U_\infty^2 C_D A$, with $\rho = 0.09$ kg/m^3 obtained from RPA simulations estimating the thermodynamic properties of the exhaust gas, $U_\infty = 2000$ m/s obtained from CFD analysis, and C_D obtained from prior experimental studies on flow around cylinders at various Reynolds numbers[94]. For a Reynolds number of $\mathrm{Re} = \rho U_\infty D/\mu \simeq 3.5 \cdot 10^6$, the flow lies in the critical transition regime between laminar and turbulent boundary layers. In this regime, the drag coefficient fluctuates in the range $C_D \in [0.3, 0.6]$ (Fig. 8), which results in a drag force ranging from $F_D \in [13\,824, 27\,648]$ N. This corresponds to a distributed load along the probe of $q \in [8\,640, 17\,280]$ N/m. Since F_D and Re scale with ρ, μ, and U_∞, the accuracy of the estimated structural loads is directly dependent on the precision of the CFD and RPA simulations. Furthermore, the formulation of F_D assumes a perfectly uniform flow around the cylindrical probe, which may not hold in reality due to the presence of turbulent structures and ground effects near the exhaust exit. These effects may locally reduce the flow velocity, particularly near the base of the probe, suggesting that the actual aerodynamic force may be lower than predicted. To maintain conservative safety margins, the upper bound of the distributed load $q = 17\,280$ N/m was retained for structural simulation. These simulations, conducted on pure refractory metals listed in Table 3, indicated that probes made of pure tantalum or niobium would exhibit little to no margin before yielding. On average, a maximum stress of approximately $\sigma_{\max} \simeq 100$ MPa was observed, located at the fixed end of the sampling probe (Fig. 10).

The resulting counter-flow heat exchanger length of $L = 14$ m is derived from multiple variables, including the outlet coolant temperature T_{co} and the convective heat transfer coefficients of the hot and cold streams (h_h and h_c, respectively). Each of these quantities relied on simplifying assumptions that affect the fidelity of the model.
First, by applying the conservation of energy between the hot and cold flows ($\dot{Q}_h = \dot{Q}_c$), the outlet coolant

temperature T_{co} is expressed as a function of the hot gas specific heat capacity $C_{p,h}$ and the coolant mass flow rate $\dot{m}_c$. Here, $C_{p,h} = 2431.4$ J/kgK was extracted from the RPA simulation, reinforcing the reliance of the heat exchanger model on the precision of RPA-derived thermodynamic properties. The coolant mass flow rate was set to $\dot{m}_c = 2.5$ kg/s, selected because it lies at the onset of the convergence region of the function $T_{\text{co}}(\dot{m}_c)$. Although reasonable, this value was chosen empirically, and a more detailed analysis of optimal and available cooling flow rates would refine the final temperature estimate. With this configuration, the outlet nitrogen temperature was calculated to be $T_{\text{co}} = 671.96$ K.
Second, the convective coefficients h_h and h_c were estimated using the Nusselt number correlation for pipe internal flows, specifically the Dittus-Boelter equation $\text{Nu}_D = 0.023\text{Re}_D^{4/5}\text{Pr}^n$, where $\text{Nu}_D = \frac{hD}{k}$, and the Reynolds and Prandtl numbers were computed using gas properties extracted from the RPA simulations. While this correlation is widely used, it is known to not be the most efficient for industrial applications with strong temperature gradients[96], such as those encountered here. Nonetheless, using this method, convective heat transfer coefficients of $h_h = 1212.6$ W/m^{2}K and $h_c = 682.23$ W/m^{2}K were obtained.

The analysis of gas flow kinetics within the conduction pipe was performed to estimate the outlet velocity, thereby informing the required hydraulic system or auxiliary equipment needed to ensure a controlled and usable flow rate at the entrance of the storage receptacle for post-test laboratory analysis. Two primary pressure loss mechanisms were considered in this evaluation: frictional losses ΔP_L and localized losses induced by the three 90° elbows ΔP_c.
Frictional losses ΔP_L were evaluated using the Darcy-Weisbach equation, which depends on the average surface roughness of the pipe wall. A value of $\varepsilon = 11.35$ μm was adopted, corresponding to relatively high surface roughness for a pure tungsten surface[98]. While this value offers a conservative estimation, a more detailed survey of commercially available tungsten pipe roughness would refine the estimate of the frictional pressure loss, which was calculated to be $\Delta P_L = 4.4$ Pa.
Losses due to pipe elbows were computed by summing the dynamic pressure loss across each of the three bends. These localized losses were modeled using a standard loss coefficient $K = 0.3$ for 90° elbows[97]. No simplifying assumptions were introduced in the formulation of ΔP_c, making this estimate directly dependent on the accuracy of the upstream gas velocity and density extracted from the CFD and RPA simulations. Thus, the calculation results in a cumulative pressure drop of $\Delta P_c = 3K\frac{\rho U_\infty^2}{2} = 162$ MPa.
Together, these findings indicate that the outlet velocity of the gas is slightly impacted by both distributed and localized losses within the conduction network. Consequently, the design methodology must incorporate an external flow regulation device, such as a flow restrictor or pressure control valve, at the end of the conduction pipe to ensure stable and predictable flow conditions into the storage unit.

5.1.2 Budget Analysis

The production cost $\text{Cost}_{\text{Production}}$ was computed by multiplying the mass of each component of Design 1 (namely the exhaust gas conduction pipe and the counter-flow heat exchanger) by the tabulated price of the corresponding material in \$/kg. The material data, as well as the structural numerical simulations, were based solely on pure metals and did not account for industrial alloys. This methodological choice is justified by two main arguments. First, the availability of mechanical and thermal property data for pure metals is significantly greater in the literature and engineering databases, facilitating robust simulation and evaluation. Second, by establishing a baseline performance for each pure metal under the defined operating conditions, it becomes possible to assess their suitability as base materials in alloying strategies, thus guiding future alloy selection. It is also important to highlight that although the computation of $\text{Cost}_{\text{Production}}$ is based on rational theoretical assumptions and tabulated values, it does not fully reflect the practical procedures typically involved in component procurement. In reality, the production process would involve direct acquisition from suppliers, often relying on standardized tubing products, as shown in figure 22 in appendix for example. A more realistic cost estimation would therefore involve market analysis of commercially available tungsten or molybdenum pipes manufactured at the required dimensions. Considering that these materials are frequently sold in alloyed forms, a targeted study of alloy availability and pricing could potentially lead to a significant reduction in $\text{Cost}_{\text{Production}}$ while maintaining or even improving structural viability.

The estimation of the service cost $\text{Cost}_{\text{Service}}$ was based on standard reference values for underground pipe

installation provided by Ofri[100], an industrial intermediary platform that connects clients with professional service providers. The value retained in this study corresponds to the sum of average prices (mean between minimum and maximum quotations) across each installation step, as reported in Table 18. While this estimation provides a practical baseline for budgeting, several aspects must be considered regarding its representativity and accuracy. First, the reference prices compiled by Ofri are derived from historical market data within an industrial and commercial context, and may not reflect the specific conditions of academic or research-based infrastructure projects such as those carried out within the EuRoC framework. In such contexts, it is not uncommon for part of the installation work to be performed internally by technically trained members of the research team. For instance, excavation tasks or on-site logistics, such as soil transport and trench preparation, could be undertaken by members of the ERT, who possess relevant technical competencies. This internal execution has the potential to reduce the reliance on third-party contractors and thereby lower the overall service expenditure. As a result, the value of $\text{Cost}_{\text{Service}}$ used in this study is likely an overestimation, assuming a fully outsourced installation to external industrial partners. In practice, especially within the EuRoC context, a hybrid approach involving both internal manpower and external expertise is more probable, suggesting that real service costs could be notably lower.

The labor cost estimation $\text{Cost}_{\text{Labor}}$ was derived using two distinct data sources: (i) benchmark values for the labor time required to install pipelines of the intended dimensions[101] (Table 6), and (ii) median monthly wages for typical professional roles involved in underground pipeline installation[107] (Table 20). The former is based on industrial norms comparable to those provided by Ofri, while the latter aggregates salary data for skilled labor categories relevant to pipeline installation (e.g., welders, site operators). The hourly wage calculation was based on average French salaries, which implicitly assumes that the hired workforce is French. As with the estimation of service costs, this assumption does not necessarily reflect the actual labor practices in an academic or scientific environment. In such contexts, especially within student-led initiatives such as the ERT, project execution often involves team members contributing their time without financial compensation. This academic model can substantially lower real labor expenses compared to market-based estimates. Therefore, the reported value of $\text{Cost}_{\text{Labor}}$ should be interpreted as a conservative upper bound, corresponding to a scenario in which all labor tasks are outsourced to professional contractors. In practice, partial internalization of labor is expected, leading to a lower effective cost. Nonetheless, independently of who performs the tasks, the adopted methodology allowed for an estimation of total working hours required for a pipeline of the size used in the counter-flow heat exchanger. Combining both laying and welding operations, was estimated at 36 hours. This value provides a solid basis for future budgeting efforts, even if the exact cost per hour may vary depending on the labor source.

5.2 Design 2

5.2.1 Critical Review on Design Methodology

Two specific imaging devices, along with a series of secure camera depths z_{SC} as a function of axial position x, were identified to enable safe visualization of the interaction between the exhaust gas and the ambient air, without risking damage from the combustion jet. However, several important clarifications must be made regarding the reliability and robustness of these two key design outcomes.

First, the selection of imaging devices for gas visualization was based on tabulated infrared absorption bands of exhaust gas species. These species and their concentrations were derived from Rocket Propulsion Analysis (RPA) simulations. As such, the suitability and effectiveness of the chosen cameras are directly dependent on the accuracy of the species data generated by RPA.

Second, the determination of the secure distances from the jet axis relied on level curves for velocity $U = 0$ m/s and temperature $T = 277$ K from exhaust jet CFD results. These thresholds were used to identify regions beyond which the ambient conditions were fully re-established, thereby ensuring camera integrity. This methodology implies a strong dependency on the fidelity of the CFD simulations. Since the CFD model used an axisymmetric assumption, the computed flow field does not account for ground effects, which in reality increase the radial spread of the jet and introduce significant turbulence levels. Consequently, the predicted safety margins shown in Figure 19 likely underestimate the real interaction

zone, and a substantial safety factor must be incorporated when determining actual deployment distances for the imaging devices.

5.2.2 Budget Analysis

The budget estimated for Design 2 significantly exceeds that of Design 1, a result that was not initially anticipated. This discrepancy is primarily due to the high cost of the imaging devices, which are hyperspectral infrared cameras with entry-level models priced well above the total cost of the complete Design 1 system, exceeding it by roughly one third. Consequently, the overall budget is overwhelmingly dominated by $\text{Cost}_{\text{Devices}}$, rendering Design2 economically less attractive for the current application. Alternative measurement methods that target only the specific exhaust gas components, without relying on full-spectrum hyperspectral imaging, may offer more budget-friendly solutions, although they could prove more complex to implement from a technical and operational standpoint. Additionally, borrowing equipment from external laboratories or partner companies could also significantly reduce the acquisition costs of the imaging devices, thereby improving the overall affordability of Design 2.

5.3 Design Assessment Analysis

This section aims to evaluate the relevance and accuracy of the binary scoring methodology through an interpretation of the intermediate scores obtained for each 5 design dimensions. The adopted method prioritizes observable differences with a binary outcome (yes = 1, no = 0), intentionally avoiding subjective to what extent gradations. This simplification is intended to facilitate a fair and transparent comparison of the two designs. The resulting scores should ideally reflect logical and expected outcomes across the five evaluation dimensions. This section also reviews the pertinence of the context-dependent weighting scheme, whereby each dimensions coefficient is set to 0.5 if the aspect becomes negligible, 1 if it remains unchanged, and 1.5 if it gains importance. Different sets of weights are expected to yield different overall scores, highlighting the dependency of design performance on the experimental context.

Three binary criteria, evaluated independently of EPFL and its Rocket Teams infrastructure, were used to assess the integrability of the system into an existing horizontal propulsion test bench. This led to a score of 33% for Design 1 and 100% for Design 2. These values are consistent with expectations: Design 1 relies entirely on mechanical gas sampling, thus requiring structural installation or machining operations and all associated constraints. In contrast, Design 2 relies solely on optical properties, allowing remote operation and requiring minimal integration effort with the existing infrastructure.

Environmental robustness was assessed using four binary criteria. With the evaluation of those criteria as presented in Section 3.5.2, Design 1 achieved 100% while Design 2 scored 38%. Design 1 was engineered to withstand the extreme conditions of the exhaust jet and, consequently, is expected to remain robust under standard atmospheric conditions. Conversely, the performance of Design 2, relying on optical systems, naturally degrades in the presence of environmental disturbances, as commonly observed with imaging equipment.

The dimension of the operational complexity was evaluated using three binary questions. Evaluating those criteria as described in Section 3.5.3 resulted to a score of 17% for Design 1 and 67% for Design 2. This result is justified by the significant technical requirements associated with post-test sample analysis in Design 1, such as gas storage, handling, and specialized analytical instrumentation. While Design 2 incorporates advanced optical imaging, it avoids most logistical and operational burdens typically associated with physical sampling systems.

Feasibility was examined using three binary criteria. Evaluating those criteria as presented in Section 3.5.4 gives Design 1 a score of 50%, and Design 2 a score of 83%. The difference stems primarily from the industrial machining and welding requirements of Design 1. Despite Design 2's relative simplicity (mainly requiring the acquisition and placement of infrared cameras) the high unit price of such equipment slightly offsets its feasibility advantage.

Adaptability to other testing configurations was assessed using three binary questions. Both designs scored 50% and 66% respectively, using the evaluation presented in section 3.5.5. These values reflect the inherent complexity of Design 1, which involves custom-dimensioned hardware (sampling probe geometry, cooling system length, etc.) that is often tailored to a specific test bench configuration. This limits its portability across different platforms. Conversely, Design 2, built upon the infrared absorption bands of combustion products, can more easily be transposed across different propulsion systems, even if the exhaust gas composition varies.

When summing the unweighted contributions of each dimension, the overall performance scores amount to 53% for Design 1 and 69% for Design 2. These scores are independent of any specific experimental context and reflect the relative performances of the two systems from a neutral standpoint, based solely on the binary criteria and dimensions selected. Under this perspective, Design 2 demonstrates a 16% higher overall performance than Design 1. However, the 31% deviation of Design 2 from the theoretical optimum of 100% suggests that improvementsparticularly in environmental robustnesscould substantially enhance its total score.

When applying the context-specific weighting factors defined in Section 3.5.6 and summarized in Table 13, the results change notably. In the EuRoC context, the overall score for Design 1 drops to 45.13% (a decrease of 8%), while that of Design 2 rises to 77.39% (an increase of 8.64%). This widens the performance gap between the two systems to 32.26%, which corresponds to an increase of 16.26% compared to the neutral evaluation. The amplification of this difference confirms that, under the constraints specific to EuRoC (notably limited time and technical resources), Design 2 becomes significantly more favorable. This shift in performance ranking stems primarily from the increased weighting assigned to integration feasibility and ease of implementation, two dimensions where Design 2 clearly excels due to its non-invasive, optical-based architecture.

When applying the weighting coefficients corresponding to the context of academic research to the dimensional scores, the overall performance increases to 66.67% for Design1 (an increase of 13.54%) and decreases to 59.33% for Design2 (a decrease of 9.42%). This reversal results in Design1 outperforming Design2 by 7.34%, thereby emerging as the preferred solution in a research-oriented setting. This shift in relative performance is primarily attributed to the distinct nature of research environments, which, in contrast to student competitions such as EuRoC, benefit from greater access to financial, technical, and human resources. These conditions reduce the importance of dimensions such as Operational Complexity and Overall Feasibility, thus favoring more technically demanding but scientifically robust systems like Design 1. Furthermore, the relevance of adaptability to an existing horizontal test bench diminishes, as extensive facilities and infrastructure in research institutions can accommodate more complex setups, thereby loosening design constraints on integration and modularity.

6 Conclusion

6.1 Objectives

This semester project, conducted as part of a Masters program in Mechanical Engineering at EPFL, aims to design two measurement systems for characterizing the exhaust emissions of the FireHorn I rocket developed by the EPFL Rocket Team. The overarching goal is to assess the environmental impact of the launcher during horizontal static fire tests. Two complementary approaches have been proposed: the first system (Design 1) aims to sample the exhaust gases and transport them through a conduction line to a storage receptacle for post-test laboratory analysis; the second system (Design 2) focuses on the in-situ observation of gas behavior by capturing infrared images of the interaction between the exhaust plume and ambient air, calibrated based on the absorption bands of the combustion products.

In addition to the system design, a secondary objective is the preliminary budget estimation of each measurement approach. This cost assessment is intended to provide insight into how well each system aligns with the financial constraints typically encountered by the EPFL Rocket Team. A quantified cost projection can guide early feasibility decisions and help prioritize which approach is more compatible with student-led initiatives under limited funding.

Finally, since the two systems are designed to measure fundamentally different physical phenomena, a third objective is to establish a structured evaluation framework that enables a fair comparison. The goal is to determine, beyond technical feasibility alone, which approach offers the most suitable balance of performance within the intended operational context.

6.2 Summary of Key Findings

For the preliminary results, the RPA simulation provided the thermodynamic properties of the exhaust gas (see Table 2) along with its chemical composition. The resulting combustion gas mixture was found to consist of 50.9% H_2O, 20.8% CO_2, 19.1% CO, and 8.7% H_2, with the remaining fraction composed of H, O, OH, and O_2. These values served as a foundational input for both the chemical absorption analysis and the thermal design of the system. The extraction of the velocity and temperature fields revealed the presence of a shockwave at approximately $x \in [6, 8]$ cm downstream of the nozzle exit, where a sharp drop in Mach number from $\mathrm{Ma} = 4.84$ to $\mathrm{Ma} = 0.89$ was accompanied by an increase in temperature from $T = 1015$ K to $T = 3321$ K. By coupling Mach and temperature values using $U_\infty = \mathrm{Ma} \cdot \sqrt{\gamma RT/M}$, extreme flow velocities ranging from $U_\infty = 650$ m/s to $U_\infty = 5649$ m/s were obtained. In addition, a stable region was identified between $x \in [60, 160]$ cm, where the velocity remained approximately constant around $\overline{U}_\infty = 2000$ m/s and the temperature decreased gradually from $T = 2500$ K to $T = 1844$ K. This stable zone was selected as the baseline region for the mechanical and thermal design of the sampling probe.

For Design 1, the structural analysis detailed in the methodology section resulted in an estimated drag force of $F_D = 27\,648$ N, yielding a distributed load of $q = 17\,280$ N/m applied to the sampling probe. When this load was applied in the structural simulations, the resulting maximum stress observed near the clamping point reached approximately $\sigma_{\max} \simeq 100$ MPa. Based on this result, only tungsten and molybdenum among all refractory metals listed in Table3 were found to simultaneously satisfy the structural, thermal, and economic constraints. The methodology employed for the cooling design led to the selection of a coolant mass flow rate of $\dot{m}c = 2.5$ kg/s, with an inlet temperature of $T\mathrm{ci} = 100$ K. This configuration yields an outlet coolant temperature of $T_{\mathrm{co}} = 671.96$ K. The convective heat transfer coefficients for the hot and cold flows were determined, using Dittus-Boelter correlation and Nusselt number, as $h_h = 1212.6$ W/m^{2}K and $h_c = 682.23$ W/m^{2}K, respectively. These values led to the design of a counter-flow heat exchanger with a total required length of $L = 14$ m. Finally, the conduction analysis along the gas transport line, based on Bernoullis equation including frictional and minor losses, resulted in pressure losses of $\Delta P_L = 4.4$ Pa due to friction and $\Delta P_c = 162$ MPa due to the presence of three 90° elbows. Taking these losses into account and using the inlet velocity extracted from CFD simulations, the outlet gas velocity was estimated at $U_{\mathrm{out}} = 1\,923.3$ m/s.

The total volume of the exhaust gas conduction pipe and the counter-flow heat exchanger was determined to be 0.077 m^3 and 0.070 m^3, respectively. When multiplied by the material density, these values correspond to component masses of 1478.71 kg if the pipe is made of pure tungsten or 782.96 kg if made of molybdenum, and 554.07 kg for the heat exchanger (assumed to be made of steel). These masses, combined with average market prices for the materials extracted from the literature, yield an average total production cost of $\text{Cost}_{\text{Production}} = 42\,032.45$ \$. By averaging the minimum and maximum cost estimates provided by Ofri for the on-site setup operations, the implementation cost was calculated as CostService = 1621.20 \$. Labor costs were estimated by multiplying a mean hourly wage of 12.20 Euro/h (based on French workforce standards) with the total number of working hours required to install a pipeline of equivalent dimensions to Design 1. This resulted in a labor cost of CostLabor = 494.44 \$. Altogether, the total estimated budget for implementing Design 1 amounts to $\text{Budget}_{\text{D1}} = 44\,148.10$ \$, under the assumptions of unrestricted resources and the use of standard industrial procedures.

The methodology adopted for the development of Design 2 focused on two critical aspects: identifying the spectral absorption bands of the exhaust gas species and determining secure camera positioning relative to the combustion jet. Based on the exhaust gas composition estimated via RPA simulation, the dominant species identified include H_2O, CO_2, CO, H_2, and OH, with absorption bands ranging from approximately 2 μm to 7.87 μm. By cross-referencing these bands with commercially available infrared imaging systems, two camera models, FLIR X8580 and Telops FAST M2k, were selected for their compatibility with the required spectral coverage. Safe distances from the jet axis were established by extracting the iso-contours of velocity ($U = 0$ m/s) and temperature ($T = 277$ K) from 3D reconstructions of the flow field derived from previous CFD simulations. Under the assumption of axisymmetric flow, these contours provide a first-order estimate of the minimum safe depth z_{SC} for each axial position x, which in turn dictates the camera placement to ensure instrument safety during operation. Figure 16 presents the estimated safety distances z_{SC} required for camera placement along the axial direction x, ranging from 5.0cm at the nozzle exit to 25.0cm at 2 m downstream, ensuring the infrared systems remain outside the influence zone of the exhaust plume.

The comparative evaluation of both designs was conducted through binary-scoring methodology across five key dimensions: integration to test bench, environmental robustness, operational complexity, overall feasibility, and adaptability. Each dimension was assessed using 3 to 4 binary sub-criteria, which were averaged to obtain a continuous performance score. Under neutral conditions (i.e., without applying any contextual weighting factors), the following dimension scores were obtained: (i) Integration to test bench: 33% for Design1, 100% for Design2, (ii) Environmental robustness: 100% for Design1, 38% for Design2 (iii) Operational complexity: 17% for Design1, 67% for Design2 (iv) Overall feasibility: 50% for Design1, 83% for Design2 (v) Adaptability: 50% for Design1, 66% for Design2.

Averaging these dimension scores yields a global performance score of 53% for Design 1 and 69% for Design 2, indicating a 16% advantage in favor of the second system. These values are consistent with the technical characteristics of each design. Design1, based on a physically intrusive gas sampling system, involves significant mechanical integration and procedural complexity, but demonstrates strong robustness. Conversely, Design2, centered on remote infrared imaging, offers superior integration flexibility and ease of deployment, but is more sensitive to ambient environmental conditions.

Upon applying contextual weighting coefficients, defined based on the relevance of each dimension within a specific testing environment, performance scores exhibited notable variations. Under the EuRoC competition context, where resource and time constraints dominate, Design 2's score increased to 77.39%, while Design 1's score decreased to 45.13%, thus amplifying the performance gap to 32.60%. In contrast, under a scientific research context, characterized by broader technical capabilities and fewer integration limitations, Design 1 reached a performance score of 66.67%, outperforming Design 2, which dropped to 59.33%. These findings highlight the strong influence of operational context in determining which system is best suited to meet experimental goals.

6.3 Limitations and Assumptions

The accuracy and relevance of the two designs developed in this study are directly constrained by the quality of the CFD and RPA simulations. Since these tools inform the entire design methodology, both in terms of the flow conditions (velocity and temperature fields) and chemical composition, the reliability of the proposed systems is ultimately based on the reliability of these simulations.

The CFD results, in particular, are based on the assumption of an axisymmetric flow, neglecting ground effects. This assumption introduces uncertainty in the estimation of the distributed load acting on the sampling probe, ($q \propto U_\infty^2$). Indeed, the distributed load is calculated under the assumption of a fully uniform flow around the probe. In reality, the flow slows down in proximity to the ground, resulting in a drag force, and consequently a distributed load, lower than the theoretical estimate. Furthermore, the same CFD results are used to compute the outlet temperature of the coolant in the heat exchanger, ($T_{\text{co}} \propto U_\infty, , T_{\text{hi}}$). They are also involved in the estimation of the Nusselt number, through the Dittus-Boelter correlation ($\text{Nu} \propto U_\infty^{4/5}$), meaning that the final exchanger length is consequently sensitive to the velocity U_∞ and temperature T_{hi} determined from the CFD simulation. Additionally, U_∞ directly affects the estimation of pressure losses in the conduction network, with $\Delta P_L \propto U_\infty^2$ and $\Delta P_L \propto \log\left(1/U_\infty^{0.9}\right)^{-2}$ through the Darcy friction factor. This propagates to the estimation of the outlet velocity via Bernoullis equation, i.e. $U_{\text{out}} \propto \sqrt{U_\infty}, , \Delta P_L$. As for Design 2, the camera safety depths were extracted from contour plots of velocity and temperature fields, also obtained from the axisymmetric CFD model. As such, they do not account for ground effects or the intense turbulence characteristic of high-velocity jets. These effects tend to enlarge the near-ground plume diameter, implying that the true safety distance is likely greater than the values extracted from the simulation.

Several key assumptions stem from the Rocket Propulsion Analysis (RPA) simulation, which was used to estimate the thermodynamic and transport properties of the exhaust gas. These properties significantly influence the design of both measurement systems. First, the exhaust gas density ρ provided by RPA directly affects the estimation of the distributed load on the sampling probe through the relation $q \propto \rho$. Furthermore, the specific heat capacity C_p, dynamic viscosity μ, density ρ, thermal conductivity k, and Prandtl number Pr were used in the thermal design of the counter-flow heat exchanger. In particular, the exchanger length is functionally dependent on these quantities, ($L \propto C_p, \rho, \mu, \text{Pr}, k$), meaning that any deviation or inaccuracy in the RPA predictions directly impacts the exchanger sizing. Additionally, the same density ρ contributes to the estimation of the outlet velocity of the exhaust gas from the conduction pipe, via Bernoullis law, where $U_{\text{out}} \propto \sqrt{\rho}$. Finally, in the context of Design 2, the spectral absorption bands of the exhaust-gas constituents, used to define the required detection range of the infrared imaging systems, were derived entirely from the chemical composition predicted by the RPA. As such, the resulting spectral window $\nu \in [2, 7.87]\mu\text{m}$ is directly tied to the fidelity of the RPAs chemical output.

The budget estimation for Design 1 was based on several major assumptions. First, the production cost $\text{Cost}_{\text{Production}}$ was calculated by multiplying the total mass of each subsystem by the average cost per kilogram of the materials involved. While this provides a reasonable first-order theoretical estimate, a more accurate and realistic calculation would require a dedicated market survey of commercially available piping components. Such a study would not only improve financial accuracy by incorporating actual supplier pricing, delivery fees, and availability, but also provide information on pre-processing requirements (e.g., machining, surface finishing) that could further affect the overall cost. Moreover, the cost of site setup $\text{Cost}_{\text{Service}}$ and labor charges $\text{Cost}_{\text{Labor}}$ were both estimated using reference tables from intermediary companies. Although this approach aligns with a scientific and consistent estimation methodology, a more robust strategy would rely on official state-published labor databases and multiple service provider quotations to establish a credible pricing range. Additionally, these cost estimation assume that the entirety of the system installation is outsourced to external professional services. In the specific context of EuRoC, many of these tasks would likely be carried out by internal members of the EPFL Rocket Team, significantly reducing actual implementation costs. Regarding Design 2, the budget evaluation was based solely on the integration of high-end infrared cameras for spectral imaging. While this provides a reliable benchmark for cost, it neglects the potential for lower-cost alternatives or hybrid systems that may satisfy performance

requirements at a fraction of the expense. Future iterations should consider such alternatives to reassess the financial feasibility of Design 2.

The design assessment methodology employed in this study relies on a binary scoring framework applied to five key evaluation dimensions. While the binary criteria selected for each dimension produced consistent and logical aggregated scores, certain limitations remain. In particular, some criteria were assigned partial scores (e.g. 0.5 out of 1) in cases where a condition was only partially satisfied or subject to a threshold. Although this allowed for greater nuance, it also introduced subjectivity into what was originally intended as a binary evaluation system. Furthermore, each dimension was assessed using only three to four binary criteria. This limited number of inputs may not fully capture the complexity of each dimension, thereby reducing the realism of the evaluation. Finally, the application of context-dependent weighting coefficients successfully demonstrated how performance rankings shift under different experimental conditions (e.g., EuRoC vs. academic research), but these global performance scores remain constrained by the limited scope of the five predefined dimensions. A more comprehensive multi-criteria framework might yield a more accurate and holistic comparison between designs.

6.4 Recommendation for Future Work

Given that the design of both measurement systems relies heavily on numerical simulations, a more rigorous reliability analysis of the CFD and RPA results is recommended. For Design 1 in particular, which is sensitive to flow velocity, temperature, and mechanical loads, improving the fidelity of the CFD model could significantly enhance design accuracy. This could be achieved by incorporating ground effects, refining turbulence modeling, and transitioning from an axisymmetric to a fully 3D simulation. Similarly, the accuracy of the RPA software could be assessed by simulating a known propulsion system and comparing its predictions with experimentally validated data.

Knowing the outlet velocity of the exhaust gas at the end of the conduction pipe opens the possibility to model the downstream system, comprising both the flow control device and the hermetically sealed storage receptacle, based on the physical and operational constraints associated with these components. This modeling effort would enable the design of a flow regulation mechanism that ensures controlled entry into the storage system. The design of the receptacle should focus on material selection and dimensional requirements to ensure gas preservation in an inert environment, thereby maintaining its original composition for post-test analysis.

Regarding budget estimation, the production cost assessment could be substantially improved through a supplier market study. Since most suppliers do not publicly list their catalog prices, a more realistic cost estimate would require the collection of multiple quotations through direct contact. This approach would not only provide a better understanding of actual costs but also account for the availability of high-temperature piping solutions and any required pre-processing (e.g., surface finishing or machining). Additionally, in the specific context of EuRoC, a tailored budget analysis could be conducted by investigating the rental costs of required equipment, especially for excavation and material handling, alongside the potential for labor substitution. For Design 2, which currently relies exclusively on hyperspectral cameras as optical equipment, it is recommended to conduct a comparative analysis of alternative sensors and imaging systems. Exploring potentially less expensive options could significantly reduce the overall budget for Design 2 without compromising the objectives of the study.

Finally, to refine the evaluation of the two designs, it is recommended to expand and nuance the current binary scoring method. Introducing graded scores for threshold-based criteria would allow for more continuous and realistic assessments. Moreover, increasing the number of criteria and evaluation dimensions could enhance the realism of the design comparison and potentially uncover additional strengths and weaknesses specific to each system. This would pave the way for a more robust and comprehensive decision-making process.

References

[1] Charles H. Jackman, David B. Considine, and Eric L. Fleming. "Space shuttle's impact on the stratosphere: An update". In: *Journal of Geophysical Research: Atmospheres* 101.D7 (1996), pp. 12523–12529. DOI: https://doi.org/10.1029/96JD00577. URL: https://agupubs.onlinelibrary.wiley.com/doi/abs/10.1029/96JD00577.

[2] A. E. Jones, S. Bekki, and J. A. Pyle. "On the atmospheric impact of launching the Ariane 5 rocket". en. In: *Journal of Geophysical Research: Atmospheres* 100.D8 (Aug. 1995), pp. 16651–16660. ISSN: 0148-0227. DOI: 10.1029/95JD01539. URL: https://agupubs.onlinelibrary.wiley.com/doi/10.1029/95JD01539 (visited on 02/18/2025).

[3] M. Y. Danilin et al. "Global stratospheric effects of the alumina emissions by solidfueled rocket motors". en. In: *Journal of Geophysical Research: Atmospheres* 106.D12 (June 2001), pp. 12727–12738. ISSN: 0148-0227. DOI: 10.1029/2001JD900022. URL: https://agupubs.onlinelibrary.wiley.com/doi/10.1029/2001JD900022 (visited on 02/18/2025).

[4] Martin N. Ross and Patti M. Sheaffer. "Radiative forcing caused by rocket engine emissions". en. In: *Earth's Future* 2.4 (Apr. 2014), pp. 177–196. ISSN: 2328-4277, 2328-4277. DOI: 10.1002/2013EF000160. URL: https://agupubs.onlinelibrary.wiley.com/doi/10.1002/2013EF000160 (visited on 02/18/2025).

[5] J. A. Dallas et al. "The environmental impact of emissions from space launches: A comprehensive review". In: *Journal of Cleaner Production* 255 (2020), p. 120209. ISSN: 0959-6526. DOI: https://doi.org/10.1016/j.jclepro.2020.120209. URL: https://www.sciencedirect.com/science/article/pii/S0959652620302560.

[6] Martin Ross, Michael Mills, and Darin Toohey. "Potential climate impact of black carbon emitted by rockets". en. In: *Geophysical Research Letters* 37.24 (Dec. 2010), 2010GL044548. ISSN: 0094-8276, 1944-8007. DOI: 10.1029/2010GL044548. URL: https://agupubs.onlinelibrary.wiley.com/doi/10.1029/2010GL044548 (visited on 02/18/2025).

[7] Christopher M Maloney et al. "The Climate and Ozone Impacts of Black Carbon Emissions From Global Rocket Launches". en. In: *Journal of Geophysical Research: Atmospheres* 127.12 (June 2022), e2021JD036373. ISSN: 2169-897X, 2169-8996. DOI: 10.1029/2021JD036373. URL: https://agupubs.onlinelibrary.wiley.com/doi/10.1029/2021JD036373 (visited on 02/18/2025).

[8] Martin Ross, Michael Mills, and Darin Toohey. "Potential climate impact of black carbon emitted by rockets". en. In: *Geophysical Research Letters* 37.24 (Dec. 2010), 2010GL044548. ISSN: 0094-8276, 1944-8007. DOI: 10.1029/2010GL044548. URL: https://agupubs.onlinelibrary.wiley.com/doi/10.1029/2010GL044548 (visited on 02/18/2025).

[9] V. Ramanathan and G. Carmichael. "Global and regional climate changes due to black carbon". en. In: *Nature Geoscience* 1.4 (Apr. 2008), pp. 221–227. ISSN: 1752-0894, 1752-0908. DOI: 10.1038/ngeo156. URL: https://www.nature.com/articles/ngeo156 (visited on 02/18/2025).

[10] Johannes Friedrich Pletzer et al. *The Climate Impact of Hypersonic Transport*. May 2022. DOI: 10.5194/egusphere-2022-285. URL: https://egusphere.copernicus.org/preprints/2022/egusphere-2022-285/ (visited on 02/18/2025).

[11] P. Gray and M. Spencer. "Combustion of unsymmetrical dimethyl hydrazine: Spontaneous ignition in decomposition and oxidation". In: *Combustion and Flame* 6 (1962), pp. 337–345. ISSN: 0010-2180. DOI: https://doi.org/10.1016/0010-2180(62)90111-6. URL: https://www.sciencedirect.com/science/article/pii/0010218062901116.

[12] Biswajit Roy and Subhajit Bandyopadhyay. "The design strategies and mechanisms of fluorogenic and chromogenic probes for the detection of hydrazine". en. In: *Analytical Methods* 10.10 (2018), pp. 1117–1139. ISSN: 1759-9660, 1759-9679. DOI: 10.1039/C7AY02866K. URL: https://xlink.rsc.org/?DOI=C7AY02866K (visited on 02/18/2025).

[13] Lars Carlsen, Olga A. Kenesova, and Svetlana E. Batyrbekova. "A preliminary assessment of the potential environmental and human health impact of unsymmetrical dimethylhydrazine as a result of space activities". en. In: *Chemosphere* 67.6 (Apr. 2007), pp. 1108–1116. ISSN: 00456535. DOI: 10.1016/j.chemosphere.2006.11.046. URL: https://linkinghub.elsevier.com/retrieve/pii/S0045653506016511 (visited on 02/18/2025).

[14] N.A. Davydenko et al. "Hybrid rocket engines: The benefits and prospects". en. In: *Aerospace Science and Technology* 11.1 (Jan. 2007), pp. 55–60. ISSN: 12709638. DOI: 10.1016/j.ast.2006.08.008. URL: https://linkinghub.elsevier.com/retrieve/pii/S1270963806001404 (visited on 02/18/2025).

[15] Jeffrey Muss. "Appendix G - Exhaust Plume Calculations". en. In: 0 ().

[16] HS Pergament, RI Gomberg, and IG Poppoff. "NOx deposition in the stratosphere from the space shuttle rocket motors". In: *NASA Tech. Memo. X-58198* (1977).

[17] M. N. Ross et al. "Insitu measurement of Cl_2 and O_3 in a stratospheric solid rocket motor exhaust plume". en. In: *Geophysical Research Letters* 24.14 (July 1997), pp. 1755–1758. ISSN: 0094-8276, 1944-8007. DOI: 10.1029/97GL01592. URL: https://agupubs.onlinelibrary.wiley.com/doi/10.1029/97GL01592 (visited on 02/18/2025).

[18] J. Benbrook et al. "In-situ dual beam UV absorption measurement of ozone in SRM plumes". en. In: *35th Aerospace Sciences Meeting and Exhibit*. Reno,NV,U.S.A.: American Institute of Aeronautics and Astronautics, Jan. 1997. DOI: 10.2514/6.1997-528. URL: https://arc.aiaa.org/doi/10.2514/6.1997-528 (visited on 02/18/2025).

[19] M. N. Ross et al. "Observation of stratospheric ozone depletion associated with Delta II rocket emissions". en. In: *Geophysical Research Letters* 27.15 (Aug. 2000), pp. 2209–2212. ISSN: 0094-8276, 1944-8007. DOI: 10.1029/1999GL011159. URL: https://agupubs.onlinelibrary.wiley.com/doi/10.1029/1999GL011159 (visited on 02/18/2025).

[20] H. C. Pumphrey, A. Lambert, and N. J. Livesey. *Observation of the exhaust plume from the space shuttle main engine using the Microwave Limb Sounder*. Aug. 2010. DOI: 10.5194/amtd-3-3971-2010. URL: https://amt.copernicus.org/articles/4/89/2011/amt-4-89-2011-discussion.html (visited on 02/18/2025).

[21] M. N. Ross et al. "Observation of stratospheric ozone depletion in rocket exhaust plumes". en. In: *Nature* 390.6655 (Nov. 1997), pp. 62–64. ISSN: 0028-0836, 1476-4687. DOI: 10.1038/36318. URL: https://www.nature.com/articles/36318 (visited on 02/18/2025).

[22] M. N. Ross et al. "Observation of stratospheric ozone depletion in rocket exhaust plumes". en. In: *Nature* 390.6655 (Nov. 1997), pp. 62–64. ISSN: 0028-0836, 1476-4687. DOI: 10.1038/36318. URL: https://www.nature.com/articles/36318 (visited on 02/18/2025).

[23] S. Bekki et al. "Impacts of space vehicles launch re-entry on the ozone layer and climate". In: *Clean Space Industrial Days AeroThermoDynamics Design for Demise Workshop*. 2017. URL: https://indico.esa.int/event/181/contributions/1487/.

[24] Martin Ross et al. "Limits on the Space Launch Market Related to Stratospheric Ozone Depletion". en. In: *Astropolitics* 7.1 (Mar. 2009), pp. 50–82. ISSN: 1477-7622, 1557-2943. DOI: 10.1080/14777620902768867. URL: https://www.tandfonline.com/doi/full/10.1080/14777620902768867 (visited on 02/18/2025).

[25] Bernard Jeffrey Anderson and Vernon W Keller. *Space shuttle exhaust cloud properties*. Tech. rep. 1983.

[26] Thomas W Dreschel and C Ross Hinkle. "Acid deposition, pH and inorganic carbon interactions: Laboratory simulation of Space Shuttle launch cloud effects on estuarine systems". In: *NASA TM* 83094 (1984), p. 13.

[27] NOx EPA. *How Nitrogen Oxides Affect the Way We Live and Breathe*. Tech. rep. EPA-456/F-98-005, September 1998 [9], 1998.

[28] Di Price et al. *Nitrogen oxides: Impacts on public health and the environment*. Tech. rep. Environmental Protection Agency, Washington, DC (United States). Office of, 1997.

[29] P. A. Schmalzer, C. R. Hinkle, and D. Breininger. *Effects of Space Shuttle Launches STS1 Through STS9 on Terrestrial Vegetation of John F. Kennedy Space Center, Florida*. Tech. rep. 83103. National Aeronautics and Space Administration, 1985. URL: https://ntrs.nasa.gov/citations/19870011225.

[30] Paul A Schmalzer et al. *Effects of space shuttle launches STS-1 through STS-9 on terrestrial vegetation of John F. Kennedy Space Center, Florida*. Tech. rep. 1985.

[31] A. F. Bouwman et al. "A global analysis of acidification and eutrophication of terrestrial ecosystems. Water Air Soil Pollut". In: *Water, Air, and Soil Pollution* 141.1/4 (2002), pp. 349–382. ISSN: 00496979. DOI: 10.1023/A:1021398008726. URL: http://link.springer.com/10.1023/A:1021398008726 (visited on 02/18/2025).

[32] W. Landolt and Th. Keller. "Uptake and effects of air pollutants on woody plants". en. In: *Experientia* 41.3 (Mar. 1985), pp. 301–310. ISSN: 0014-4754, 1420-9071. DOI: 10.1007/BF02004490. URL: http://link.springer.com/10.1007/BF02004490 (visited on 02/18/2025).

[33] G. L. Pellett et al. "HCI in Rocket Exhaust Clouds: Atmospheric Dispersion, Acid Aerosol Characteristics, and Acid Rain Deposition". en. In: *Journal of the Air Pollution Control Association* 33.4 (Apr. 1983), pp. 304–311. ISSN: 0002-2470. DOI: 10.1080/00022470.1983.10465578. URL: http://www.tandfonline.com/doi/abs/10.1080/00022470.1983.10465578 (visited on 02/18/2025).

[34] Thomas W. Dreschel and Carlton R. Hall. "Quantification of hydrochloric acid and particulate deposition resulting from space shuttle launches at John F. Kennedy space center, Florida, USA". en. In: *Environmental Management* 14.4 (July 1990), pp. 501–507. ISSN: 0364-152X, 1432-1009. DOI: 10.1007/BF02394138. URL: http://link.springer.com/10.1007/BF02394138 (visited on 02/18/2025).

[35] Susan Solomon. "Stratospheric ozone depletion: A review of concepts and history". en. In: *Reviews of Geophysics* 37.3 (Aug. 1999), pp. 275–316. ISSN: 8755-1209, 1944-9208. DOI: 10.1029/1999RG900008. URL: https://agupubs.onlinelibrary.wiley.com/doi/10.1029/1999RG900008 (visited on 02/18/2025).

[36] Richard S Stolarski et al. "Impact of future nitrous oxide and carbon dioxide emissions on the stratospheric ozone layer". In: *Environmental Research Letters* 10.3 (Mar. 2015), p. 034011. ISSN: 1748-9326. DOI: 10.1088/1748-9326/10/3/034011. URL: https://iopscience.iop.org/article/10.1088/1748-9326/10/3/034011 (visited on 02/18/2025).

[37] Michael Y. Danilin, Malcolm K. W. Ko, and Debra K. Weisenstein. "Global implications of ozone loss in a space shuttle wake". en. In: *Journal of Geophysical Research: Atmospheres* 106.D4 (Feb. 2001), pp. 3591–3601. ISSN: 0148-0227. DOI: 10.1029/2000JD900632. URL: https://agupubs.onlinelibrary.wiley.com/doi/10.1029/2000JD900632 (visited on 02/18/2025).

[38] Charles H. Jackman, David B. Considine, and Eric L. Fleming. "A global modeling study of solid rocket aluminum oxide emission effects on stratospheric ozone". en. In: *Geophysical Research Letters* 25.6 (Mar. 1998), pp. 907–910. ISSN: 0094-8276, 1944-8007. DOI: 10.1029/98GL00403. URL: https://agupubs.onlinelibrary.wiley.com/doi/10.1029/98GL00403 (visited on 02/18/2025).

[39] M. N. Ross et al. "Ozone depletion caused by NO and H_2 O emissions from hydrazinefueled rockets". en. In: *Journal of Geophysical Research: Atmospheres* 109.D21 (Nov. 2004), 2003JD004370. ISSN: 0148-0227. DOI: 10.1029/2003JD004370. URL: https://agupubs.onlinelibrary.wiley.com/doi/10.1029/2003JD004370 (visited on 02/18/2025).

[40] Jan-Steffen Fischer and Stefanos Fasoulas. "Assessment of Launch and Re-Entry Emissions of Space Transportation Systems and Their Environmental Impact". In: Oct. 2024. DOI: 10.52202/078373-0079.

[41] M. C. Kelley et al. "Radar, lidar, and optical observations in the polar summer mesosphere shortly after a space shuttle launch". en. In: *Journal of Geophysical Research: Space Physics* 115.A5 (May 2010), 2009JA014938. ISSN: 0148-0227. DOI: 10.1029/2009JA014938. URL: https://agupubs.onlinelibrary.wiley.com/doi/10.1029/2009JA014938 (visited on 02/18/2025).

[42] Michael H. Stevens et al. "Antarctic mesospheric clouds formed from space shuttle exhaust". en. In: *Geophysical Research Letters* 32.13 (July 2005), 2005GL023054. ISSN: 0094-8276, 1944-8007. DOI: 10.1029/2005GL023054. URL: https://agupubs.onlinelibrary.wiley.com/doi/10.1029/2005GL023054 (visited on 02/18/2025).

[43] Michael H. Stevens et al. "Polar mesospheric clouds formed from space shuttle exhaust". en. In: *Geophysical Research Letters* 30.10 (May 2003), 2003GL017249. ISSN: 0094-8276, 1944-8007. DOI: 10.1029/2003GL017249. URL: https://agupubs.onlinelibrary.wiley.com/doi/10.1029/2003GL017249 (visited on 02/18/2025).

[44] Erik J. L. Larson et al. "Global atmospheric response to emissions from a proposed reusable space launch system". en. In: *Earth's Future* 5.1 (Jan. 2017), pp. 37–48. ISSN: 2328-4277, 2328-4277. DOI: 10.1002/2016EF000399. URL: https://agupubs.onlinelibrary.wiley.com/doi/10.1002/2016EF000399 (visited on 02/18/2025).

[45] M. Ross and J. A. Vedda. *The Policy and Science of Rocket Emissions*. 2018. URL: https://aerospace.org/sites/default/files/2018-05/RocketEmissions_0.pdf.

[46] James M. Russell et al. "Analysis of northern midlatitude noctilucent cloud occurrences using satellite data and modeling: Mid-latitude Noctilucent Clouds". en. In: *Journal of Geophysical Research: Atmospheres* 119.6 (Mar. 2014), pp. 3238–3250. ISSN: 2169897X. DOI: 10.1002/2013JD021017. URL: http://doi.wiley.com/10.1002/2013JD021017 (visited on 02/18/2025).

[47] D. E. Siskind et al. "Signatures of shuttle and rocket exhaust plumes in TIMED/SABER radiance data". en. In: *Geophysical Research Letters* 30.15 (Aug. 2003), 2003GL017627. ISSN: 0094-8276, 1944-8007. DOI: 10.1029/2003GL017627. URL: https://agupubs.onlinelibrary.wiley.com/doi/10.1029/2003GL017627 (visited on 02/18/2025).

[48] Michael H. Stevens et al. "The polar mesospheric cloud mass in the Arctic summer". en. In: *Journal of Geophysical Research: Space Physics* 110.A2 (Feb. 2005), 2004JA010566. ISSN: 0148-0227. DOI: 10.1029/2004JA010566. URL: https://agupubs.onlinelibrary.wiley.com/doi/10.1029/2004JA010566 (visited on 02/18/2025).

[49] Ch. Voigt, U. Schumann, and K. Graf. "Contrail formation in the tropopause region caused by emissions from an Ariane 5 rocket". In: *Progress in Propulsion Physics*. Ed. by M. Calabro et al. Munich, Germany: EDP Sciences, 2016, pp. 183–196. ISBN: 978-5-94588-191-4. DOI: 10.1051/eucass/201608183. URL: http://www.eucass-proceedings.eu/10.1051/eucass/201608183 (visited on 02/18/2025).

[50] MK Nauryzbaev et al. "Ecological problems of central Asia resulting from space rocket debris". In: *History and Society in Central and Inner Asia, Toronto Studies in Central and Inner Asia* 7 (2005). Publisher: Asian Institute, University of Toronto Toronto, pp. 327–349.

[51] A MacDiarmid et al. "Marine Ecologial Risk Assessment of the cumulative impact of Electron Rocket launches". In: *Report prepared for Ministry for the Environment, National Insitute of Water and Atmospheric Research* (2016).

[52] European Space Agency. *ESA's Annual Space Environment Report*. 2021. URL: https://www.sdo.esoc.esa.int/environment_report/Space_Environment_Report_latest.pdf.

[53] Hugh G. Lewis et al. "Effect of thermospheric contraction on remediation of the near-Earth space debris environment: THERMOSPHERIC DECLINE AND SPACE DEBRIS". en. In: *Journal of Geophysical Research: Space Physics* 116.A2 (Feb. 2011), n/a–n/a. ISSN: 01480227. DOI: 10.1029/2011JA016482. URL: http://doi.wiley.com/10.1029/2011JA016482 (visited on 02/18/2025).

[54] Chul Park and John V. Rakich. "Equivalent-cone calculation of nitric oxide production rate during space shuttle re-entry". en. In: *Atmospheric Environment (1967)* 14.8 (Jan. 1980), pp. 971–972. ISSN: 00046981. DOI: 10.1016/0004-6981(80)90011-6. URL: https://linkinghub.elsevier.com/retrieve/pii/0004698180900116 (visited on 02/18/2025).

[55] John M. C. Plane, Wuhu Feng, and Erin C. M. Dawkins. "The Mesosphere and Metals: Chemistry and Changes". In: *Chemical Reviews* 115.10 (May 2015). Publisher: American Chemical Society, pp. 4497–4541. ISSN: 0009-2665. DOI: 10.1021/cr500501m. URL: https://doi.org/10.1021/cr500501m.

[56] Karl-Heinz Glassmeier et al. "The Sun, geomagnetic polarity transitions, and possible biospheric effects: review and illustrating model". In: *International Journal of Astrobiology* 8.3 (2009), pp. 147–159. DOI: 10.1017/S1473550409990073.

[57] Chul Park and John V. Rakich. "Equivalent-cone calculation of nitric oxide production rate during space shuttle re-entry". en. In: *Atmospheric Environment (1967)* 14.8 (Jan. 1980), pp. 971–972. ISSN: 00046981. DOI: 10.1016/0004-6981(80)90011-6. URL: https://linkinghub.elsevier.com/retrieve/pii/0004698180900116 (visited on 02/18/2025).

[58] James Beck et al. *Aerothermodynamic Assessment of Atmospheric Emissions from Re-entry Demise*. Technical Report. Tech. Rep. European Space Agency (ESA), 2014.

[59] Leonard Schulz and Karl-Heinz Glassmeier. "On the anthropogenic and natural injection of matter into Earths atmosphere". en. In: *Advances in Space Research* 67.3 (Feb. 2021), pp. 1002–1025. ISSN: 02731177. DOI: 10.1016/j.asr.2020.10.036. URL: https://linkinghub.elsevier.com/retrieve/pii/S0273117720307663 (visited on 02/18/2025).

[60] Aaron C. Boley and Michael Byers. "Satellite mega-constellations create risks in Low Earth Orbit, the atmosphere and on Earth". en. In: *Scientific Reports* 11.1 (May 2021), p. 10642. ISSN: 2045-2322. DOI: 10.1038/s41598-021-89909-7. URL: https://www.nature.com/articles/s41598-021-89909-7 (visited on 02/18/2025).

[61] M. Richard Denison et al. "Solid rocket exhaust in the stratosphere - Plume diffusion and chemical reactions". en. In: *Journal of Spacecraft and Rockets* 31.3 (May 1994), pp. 435–442. ISSN: 0022-4650, 1533-6794. DOI: 10.2514/3.26457. URL: https://arc.aiaa.org/doi/10.2514/3.26457 (visited on 02/18/2025).

[62] PF Zittel. *Computer model predictions of the local effects of large, solid-fuel rocket motors on stratospheric ozone. Technical report*. Tech. rep. Aerospace Corp., El Segundo, CA (United States), 1994.

[63] J. C. McDowell. *General Catalog of Artificial Space Objects Release 1.5.4*. Accessed: 2025-04-23. 2024.

[64] J. T. Emmert et al. "NRLMSIS 2.0: A WholeAtmosphere Empirical Model of Temperature and Neutral Species Densities". en. In: *Earth and Space Science* 8.3 (Mar. 2021), e2020EA001321. ISSN: 2333-5084, 2333-5084. DOI: 10.1029/2020EA001321. URL: https://agupubs.onlinelibrary.wiley.com/doi/10.1029/2020EA001321 (visited on 02/18/2025).

[65] Michael M. James, Shane V. Lympany, Alexandria R. Salton, Matthew F. Calton, Blue Ridge Research and Consulting, LLC et al. *Commercial Space Vehicle Emissions Modeling*. Pages: 26142. Washington, D.C.: Transportation Research Board, Apr. 2021. ISBN: 978-0-309-46888-6. DOI: 10.17226/26142. URL: https://www.nap.edu/catalog/26142 (visited on 02/18/2025).

[66] Chul Park and John V. Rakich. "Equivalent-cone calculation of nitric oxide production rate during space shuttle re-entry". en. In: *Atmospheric Environment (1967)* 14.8 (Jan. 1980), pp. 971–972. ISSN: 00046981. DOI: 10.1016/0004-6981(80)90011-6. URL: https://linkinghub.elsevier.com/retrieve/pii/0004698180900116 (visited on 02/18/2025).

[67] S. Gordon and B. J. McBride. *Computer program for calculation of complex chemical equilibrium compositions and applications. Part 1: Analysis*. Tech. Rep. 1311. Cleveland, OH, United States: NASA Lewis Research Center, Oct. 1994.

[68] Software and Engineering Associates. *Viscous Interaction Performance Evaluation Routine For Two-Phase Nozzle Flows With Finite Rate Chemistry, VIPER 5.0*. Accessed: 2025-04-23. Carson City, NV, 2021.

[69] Sierra Engineering & Software, Inc. *Performance Correlation Program (PERCORP) Reference and User's Manual, Version 3.1.1*. Sacramento, CA, Mar. 2022.

[70] M.W. Taylor and H.S. Pergament. *Standardized Plume Flowfield Model SPF-III, Version 4.2 Program User's Manual, PST TR-51*. East Windsor, NJ, June 2000.

[71] Thibault Andriot. *B1 Engine Plume CFD Analysis*. Doc ID: 2024-C-FD-B1-ENGINE-PLUME. EPFL Rocket Team, ME-474 Numerical Flow Simulation. Dec. 2024. URL: insert%20URL%20if%20available.

[72] Wikipedia contributors. *Refractory metals*. Accessed: 2024-05-15. 2024. URL: https://en.wikipedia.org/wiki/Refractory_metals.

[73] John R. Rumble, Thomas J. Bruno, and Maria J. Doa. *CRC Handbook of Chemistry and Physics: A Ready Reference Book of Chemical and Physical Data*. 103rd ed. Boca Raton, FL: CRC Press, 2022. Chap. Section 4, p. 40. ISBN: 978-1-032-12171-0.

[74] AZoM. *Properties of Refractory Metals: Part I Introduction*. Accessed: 2024-05-15. 2006. URL: https://www.azom.com/article.aspx?ArticleID=1824.

[75] Wikipedia contributors. *Chromium*. Accessed: 2024-05-15. 2024. URL: https://en.wikipedia.org/wiki/Chromium.

[76] AZoM. *Chromium Mechanical and Physical Properties*. Accessed: 2024-05-15. 2003. URL: https://www.azom.com/properties.aspx?ArticleID=614.

[77] AZoM. *Molybdenum Mechanical and Physical Properties*. Accessed: 2024-05-15. 2006. URL: https://www.azom.com/properties.aspx?ArticleID=1491.

[78] AZoM. *Tungsten Mechanical and Physical Properties*. Accessed: 2024-05-15. 2007. URL: https://www.azom.com/properties.aspx?ArticleID=1842.

[79] MIT Materials Properties. *Tungsten*. Accessed: 2024-05-15. URL: https://www.mit.edu/~6.777/matprops/tungsten.htm.

[80] Wikipedia contributors. *Rhenium*. Accessed: 2024-05-15. 2024. URL: https://en.wikipedia.org/wiki/Rhenium.

[81] John W. Arblaster. *Selected Values of the Crystallographic Properties of Elements*. Materials Park, Ohio: ASM International, 2018. ISBN: 978-1-62708-155-9.

[82] Wikipedia contributors. *Osmium*. Accessed: 2024-05-15. 2024. URL: https://en.wikipedia.org/wiki/Osmium.

[83] eFineametals. *Tantalum Properties Rod, Sheet, Foil, Coil Strip*. Accessed: 2024-05-15. URL: https://www.efineametals.com/refractory-metal-supplier/tantalum-rod-sheet-foil-coil-strip/tantalum-properties/.

[84] Glemco Metals. *Molybdenum Material Expertise*. Accessed: 2024-05-15. URL: https://www.glemco.com/capabilities/material-expertise/molybdenum/.

[85] AZoM. *Tantalum Mechanical and Physical Properties*. Accessed: 2024-05-15. 2004. URL: https://www.azom.com/properties.aspx?ArticleID=616.

[86] WHS Sondermetalle. *Niobium (Nb) Technical Data Sheet*. https://www.whs-sondermetalle.de/images/pdf/Nb-Niobium.pdf. Accessed: 2024-05-15.

[87] Wikipedia contributors. *Niobium*. Accessed: 2024-05-15. 2024. URL: https://en.wikipedia.org/wiki/Niobium.

[88] MIT Materials Properties. *Chromium*. Accessed: 2024-05-15. URL: https://www.mit.edu/~6.777/matprops/chromium.htm.

[89] Federal Institute for Geosciences and Natural Resources. *Preismonitor*. Report (PDF). Archived (PDF) from the original on 2020-01-25. Germany, Jan. 2020.

[90] Shanghai Metals Market. *Rhenium*. Archived from the original on 2020-02-03. Feb. 2020. URL: https://price.metal.com/.

[91] Osmium. *Osmium: Preis*. Retrieved 2025-04-10. 2025.

[92] Institute of Rare Earths and Metals. *Current Prices of Strategic Metals*. Archived from the original on 2020-01-14. July 2019.

[93] Shanghai Metals Market. *Niobium*. Archived from the original on 2020-02-03. Feb. 2020. URL: https://price.metal.com/.

[94] Author(s). *Incompressible Flow*. New York: Wiley-Interscience, 1984.

[95] Frank P. Incropera and David P. DeWitt. *Fundamentals of Heat and Mass Transfer*. 6th. Hoboken, NJ: Wiley, 2011.

[96] Wikipedia contributors. *Nusselt number*. Accessed: 2025-05-02. 2025. URL: https://en.wikipedia.org/wiki/Nusselt_number.

[97] The Engineering Toolbox. *Minor Loss Coefficients Pipes*. Accessed: 2025-05-15. 2025. URL: https://www.engineeringtoolbox.com/minor-loss-coefficients-pipes-d_626.html.

[98] Tae Hyun Kwon et al. "Study on sputtering yield of tungsten with different particle sizes: Surface roughness dependence". In: *Nuclear Engineering and Technology* 53.6 (2021), pp. 1939–1941. DOI: 10.1016/j.net.2020.12.024. URL: https://doi.org/10.1016/j.net.2020.12.024.

[99] Wikipedia contributors. *Moody chart*. Accessed: 2025-05-15. 2025. URL: https://en.wikipedia.org/wiki/Moody_chart.

[100] Ofri. *Excavation Costs*. https://www.ofri.ch/fr/couts/excavation. [Online; accessed 17 May 2025]. 2025.

[101] The Project Estimate. *Pipe Installation Man Hours*. Accessed: 2025-05-20. 2024. URL: https://www.theprojectestimate.com/pipe-installation-man-hours/.

[102] Kazuo Nakamoto. *Infrared and Raman Spectra of Inorganic and Coordination Compounds. Part A*. 5th. Wiley, 1997. ISBN: 978-0-471-16394-7.

[103] Forter. *IR Absorption Spectroscopy*. https://www.forter.com.tw/zh-tw/a4-10998-12310/IR-Absorption-Spectroscopy.html. Accessed: 2025-05-09.

[104] Alain Campargue et al. "The absorption spectrum of H_2: CRDS measurements of the (20) band, review of the literature data and accurate *ab initio* line list up to 35000 cm^{-1}". In: *Phys. Chem. Chem. Phys.* 14 (2012), pp. 802–815. DOI: 10.1039/C1CP22912E.

[105] Alfonso Blázquez-Castro. "Direct $1O_2$ optical excitation: A tool for redox biology". In: *Redox Biology* 13 (2017), pp. 39–59. DOI: 10.1016/j.redox.2017.05.011.

[106] *Tang Shan (Pig Iron)*. https://price.metal.com. Shanghai Metals Market. Archived from the original on 2020-02-03. Feb. 2020.

[107] Top-Métiers. *Pose de canalisations : salaires et débouchés*. Accessed: 2025-05-27. 2024. URL: https://www.top-metiers.fr/pose-canalisations.

A Appendix

A.1 Supplier's Proposal for Tungsten Probe

Figure 22: Tungsten tubes proposed by *Luoyang Combat Tungsten & Molybdenum Material Co., Ltd.* for the fabrication of the sampling probe

A.2 Supplier's Proposal for Hyperspectral Cameras

Figure 23: Hyperspectral cameras suitable for exhaust gas component detection: (a) Telops FAST M2k, (b) FLIR A6750 InSb, (c) FLIR A8580 InSb, and (d) FLIR X6980/X8580 InSb

A.3 Design 1 : Probe drag force by CFD computation

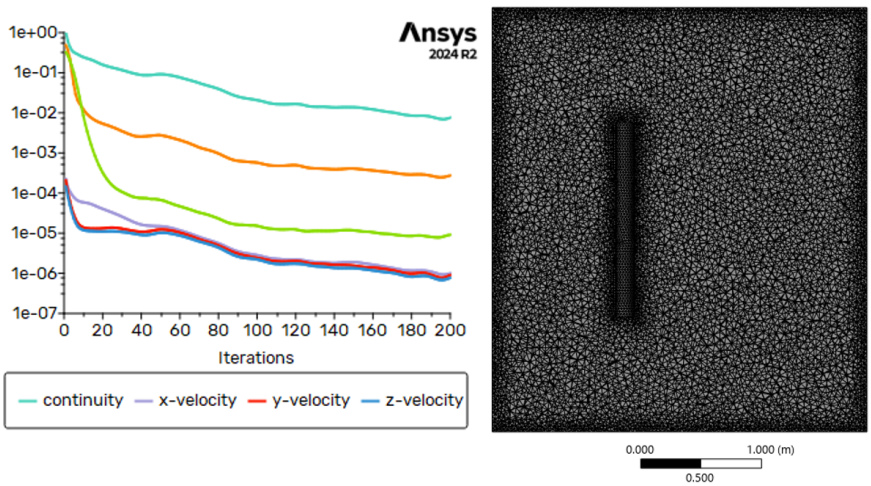

Figure 24: Residuals (left) and Mesh (right) used for drag force computation

A.4 RPA Simulation

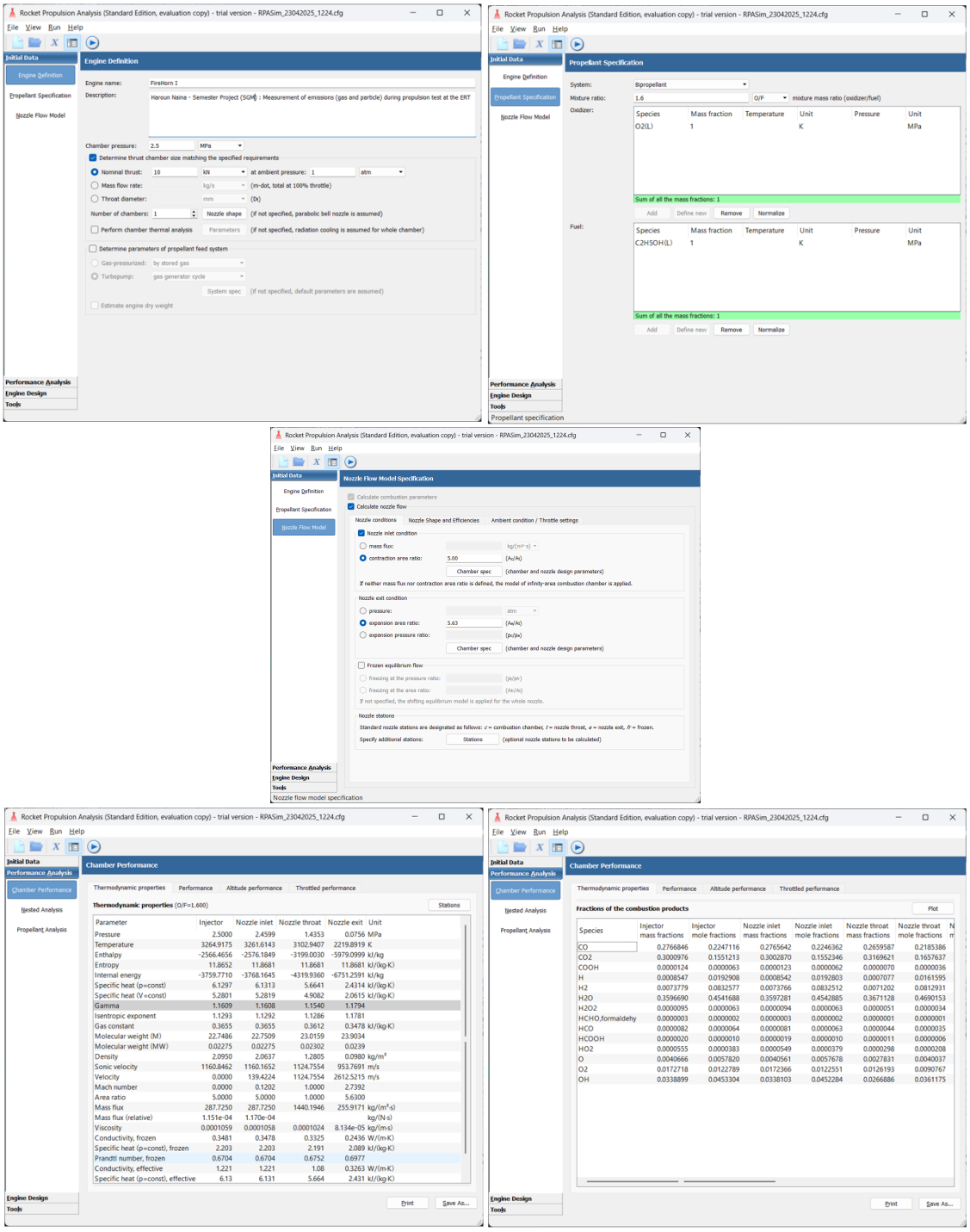

Figure 25: Input parameters (top and middle) and output results (bottom).

A.5 Axial Flow Field

```
clear all; close all; clc;

% === Paramètres d'entrée ===
mach_img_path = 'MachContour.PNG';
temp_img_path = 'TempContour.PNG';

mach_min = 4.6e-5;
mach_max = 5.04;
temp_min = 277;
temp_max = 4120;

mach_length_cm = 203.04;
temp_length_cm = 214.03;

gamma = 1.2;
r = 376.1;

% === Charger les images ===
mach_img = imread(mach_img_path);
temp_img = imread(temp_img_path);

% === Extraire une ligne horizontale proche du bas ===
line_index_mach = size(mach_img, 1) - 4;
line_index_temp = size(temp_img, 1) - 4;
mach_line_rgb = double(squeeze(mach_img(line_index_mach, :, :)));
temp_line_rgb = double(squeeze(temp_img(line_index_temp, :, :)));

% === Conversion des lignes RGB en données physiques ===
mach_values = rgb_to_scalar_jet(mach_line_rgb, mach_min, mach_max);
temp_values = rgb_to_scalar_jet(temp_line_rgb, temp_min, temp_max);

x_mach = linspace(0, mach_length_cm, length(mach_values));
x_temp = linspace(0, temp_length_cm, length(temp_values));

% === Tronquer les données pour ne conserver que x <= 200 cm ===
x_max = 200;  % Limite maximale pour x

% Filtrage des données qui dépassent x_max
x_mach = x_mach(x_mach <= x_max);
x_temp = x_temp(x_temp <= x_max);
mach_values = mach_values(1:length(x_mach));
temp_values = temp_values(1:length(x_temp));

% === Interpolation température sur la grille Mach ===
temp_interp = interp1(x_temp, temp_values, x_mach, 'linear', 'extrap');
temp_interp = temp_interp(:);  % Assure que T interpolée est un vecteur
    colonne

% === Calcul de la vitesse ===
U = mach_values .* sqrt(gamma * r * temp_interp);

% === Affichage des résultats ===
```

```
% === FIGURE 1 : Mach ===
figure;
plot(x_mach, mach_values, 'k');
xlabel('$x \;[\textrm{cm}]$','Interpreter','latex');
ylabel('$Ma(x)$','Interpreter','latex');
title('$Ma(x) \; \textrm{at} \; y=0 \; \textrm{(center exhaust)}$','
    Interpreter','latex');
grid on;
% Set figure size to a rectangular shape (e.g., 6x4)
set(gca, 'Position', [0.15, 0.15, 0.8, 0.4]);

% === FIGURE 2 : Température ===
figure;
plot(x_temp, temp_values, 'k');
xlabel('$x \; [\textrm{cm}]$','Interpreter','latex');
ylabel('$T(x) \; [\textrm{K}]$' ,'Interpreter','latex');
title('$T(x) \; \textrm{at} \; y=0 \; \textrm{(center exhaust)}$','
    Interpreter','latex');
grid on;
% Set figure size to a rectangular shape (e.g., 6x4)
set(gca, 'Position', [0.15, 0.15, 0.8, 0.4]);

% === FIGURE 3 : Vitesse U ===
figure;
plot(x_mach, U, 'k');
xlabel('$x \;[\textrm{cm}]$','Interpreter','latex');
ylabel('$U_{\infty}(x)\; [\textrm{m/s}]$' ,'Interpreter','latex');
title('$U_{\infty}(x)=Ma\sqrt{\gamma R_s T}  \; \textrm{at} \; y=0 \; \
    textrm{(center exhaust)}$','Interpreter','latex');
grid on;
% Set figure size to a rectangular shape (e.g., 6x4)
set(gca, 'Position', [0.15, 0.15, 0.8, 0.4]);

% === Fonction à la fin ===
function values = rgb_to_scalar_jet(rgb_line, vmin, vmax)
    cmap = 255 * jet(256);  % Garder en double
    n_colors = size(cmap, 1);
    values = zeros(size(rgb_line,1),1);

    for i = 1:size(rgb_line,1)
        color = rgb_line(i, :);
        [~, idx] = min(sum((cmap - color).^2, 2));
        values(i) = vmin + (idx - 1) / (n_colors - 1) * (vmax - vmin);
    end
end
```

A.6 Spatial Flow Field

```
clear; close all; clc;

% Paramètres
mach_img_path    = 'MachContour.PNG';
temp_img_path    = 'TempContour.PNG';
mach_min         = 4.6e-5;
```

```
mach_max          = 5.04;
temp_min          = 277;
temp_max          = 4120;
mach_length_cm    = 203.04;
mach_height_cm    = 50;
temp_length_cm    = 214.03;
temp_height_cm    = 50;
gamma             = 1.1794;
R                 = 347.8;
y_max_plot        = 40;

% Lecture des images
Im = double(imread(mach_img_path));
It = double(imread(temp_img_path));
[n_my, n_mx, ~] = size(Im);
[n_ty, n_tx, ~] = size(It);

% Détection des couleurs de fond (bleu uniforme)
pixelsM = reshape(Im, [], 3);
[uniqM, ~, icM] = unique(pixelsM, 'rows');
cntM    = accumarray(icM, 1);
[~, imaxM] = max(cntM);
rgb_bg_M = uniqM(imaxM, :);

pixelsT = reshape(It, [], 3);
[uniqT, ~, icT] = unique(pixelsT, 'rows');
cntT    = accumarray(icT, 1);
[~, imaxT] = max(cntT);
rgb_bg_T = uniqT(imaxT, :);

% Grilles physiques
x_m = linspace(0, mach_length_cm, n_mx);
y_m = linspace(0, mach_height_cm, n_my);
x_t = linspace(0, temp_length_cm, n_tx);
y_t = linspace(0, temp_height_cm, n_ty);

% Conversion RGB  Mach (avec fond  0)
Mach = zeros(n_my, n_mx);
for i = 1:n_my
    row = squeeze(Im(i,:,:));        % n_mxÐ3
    Mach(i,:) = rgb_to_scalar_mach(row, mach_min, mach_max, rgb_bg_M)';
end

% Conversion RGB  Temp (avec fond  temp_min)
Temp = zeros(n_ty, n_tx);
for j = 1:n_ty
    row = squeeze(It(j,:,:));
    Temp(j,:) = rgb_to_scalar_temp(row, temp_min, temp_max, rgb_bg_T)';
end

% Interpolation de Temp sur la grille Mach
Temp_on_M = zeros(n_my, n_mx);
for i = 1:n_my
    [~, iy] = min(abs(y_t - y_m(i)));
```

```
    Temp_on_M(i,:) = interp1(x_t, Temp(iy,:), x_m, 'linear', 'extrap');
end

% On inverse verticalement pour que y=0 soit en ligne 1
Mach      = flipud(Mach);
Temp_on_M = flipud(Temp_on_M);
y_m       = linspace(0, mach_height_cm, n_my);

% Calcul de U
U = Mach .* sqrt(gamma * R * Temp_on_M);

% Vérification des extrêmes
fprintf('Champ U : min = %.1f m/s, max = %.1f m/s\n', min(U(:)), max(U(:))
    );

% Extraction profils verticaux pour tracé 3D
x_plot = 0:1:200;
ix     = arrayfun(@(x0) find(abs(x_m-x0)==min(abs(x_m-x0)),1), x_plot);
y_mask = y_m <= y_max_plot;
Y_plot = y_m(y_mask);
U_plot = U(y_mask, ix);

% Tracé de la surface 3D
[X3, Y3] = meshgrid(x_plot, Y_plot);
figure('Name','Surface U(x,y)');
surf(X3, Y3, U_plot, 'EdgeColor','none');
colormap jet; colorbar;
xlabel('$x\;\mathrm{[cm]}$','Interpreter','latex');
ylabel('$y\;\mathrm{[cm]}$','Interpreter','latex');
zlabel('$U(x,y)\;\mathrm{[m/s]}$','Interpreter','latex');
title('$U(x,y)$','Interpreter','latex');
view(45,30); grid on;
set(gca, 'Position', [0.15, 0.15, 0.8, 0.4]);

% Extraction et tracé du contour U = 0 m/s
C = contourc(x_plot, Y_plot, U_plot, [0 0]);
x0 = []; y0 = []; idx = 1;
while idx < size(C,2)
    level = C(1,idx);
    npts  = C(2,idx);
    if abs(level) < 1e-6
        xs = C(1, idx+1:idx+npts);
        ys = C(2, idx+1:idx+npts);
        x0 = [x0; xs(:)];
        y0 = [y0; ys(:)];
    end
    idx = idx + npts + 1;
end
figure('Name','Courbe de niveau U=0');
plot(x0, y0, 'k-', 'LineWidth', 1);
xlabel('$x\;\mathrm{[cm]}$','Interpreter','latex');
ylabel('$y\;\mathrm{[cm]}$','Interpreter','latex');
title('Level curve : $U=0\,\mathrm{m/s}$','Interpreter','latex');
xlim([min(x_plot) max(x_plot)]);
```

```
ylim([0 y_max_plot]);
grid on;
set(gca, 'Position', [0.15, 0.15, 0.6, 0.35]);


%
    ------------------------------------------------------------------------

% Sousfonctions pour conversion RGBscalaire

function vals = rgb_to_scalar_mach(rgb_line, vmin, vmax, rgb_bg)
    cmap = 255 * jet(256);
    n = size(cmap,1);
    vals = zeros(size(rgb_line,1),1);
    for k = 1:size(rgb_line,1)
        if all(rgb_line(k,:) == rgb_bg)
            vals(k) = 0;  % fond  vitesse 0
        else
            dif = sum((cmap - rgb_line(k,:)).^2,2);
            [~, id] = min(dif);
            % rampe de mach_minmach_max
            vals(k) = vmin + (id-1)/(n-1)*(vmax-vmin);
        end
    end
end

function vals = rgb_to_scalar_temp(rgb_line, vmin, vmax, rgb_bg)
    cmap = 255 * jet(256);
    n = size(cmap,1);
    vals = zeros(size(rgb_line,1),1);
    for k = 1:size(rgb_line,1)
        if all(rgb_line(k,:) == rgb_bg)
            vals(k) = vmin;  % fond  temp_min
        else
            dif = sum((cmap - rgb_line(k,:)).^2,2);
            [~, id] = min(dif);
            vals(k) = vmin + (id-1)/(n-1)*(vmax-vmin);
        end
    end
end
```

A.7 Standard Condition Level Curve

```
clear all; close all; clc;
% Specify the filenames of your .fig files
figFile1 = 'levelCurveU.fig';
figFile2 = 'levelCurveT.fig';

% Open the first figure invisibly
fig1 = openfig(figFile1, 'invisible');
% Get the line object (assuming only one line in the axes)
ax1 = get(fig1, 'Children');
lines1 = findobj(ax1, 'Type', 'line');
% Extract X and Y data
```

```
x1 = get(lines1, 'XData');
y1 = get(lines1, 'YData');

% Open the second figure invisibly
fig2 = openfig(figFile2, 'invisible');
ax2 = get(fig2, 'Children');
lines2 = findobj(ax2, 'Type', 'line');
x2 = get(lines2, 'XData');
y2 = get(lines2, 'YData');

% Close the original figures
close(fig1);
close(fig2);

% Create a new figure for the combined plot
figure;
hold on;

% Plot both datasets
plot(x1, y1, 'k', 'LineWidth', 1);
plot(x2, y2, 'k--', 'LineWidth', 1);

% Enhance the plot
grid on;
xlabel('$x\;\mathrm{[cm]}$','Interpreter','latex');
ylabel('$y\;\mathrm{[cm]}$','Interpreter','latex');
title('Level curve : $T=277\,\mathrm{K}$ and $U=0\,\mathrm{m/s}$','
    Interpreter','latex');
legend({'$U = 0 \; \textrm{m/s}$', '$T = 277 \; \textrm{K}$'}, '
    Interpreter','latex', 'Location', 'best');
set(gca, 'Position', [0.15, 0.15, 0.6, 0.35]);

hold off;

% Optionally, save the combined figure
saveas(gcf, 'combined_plot.png');
```